NOVA SCHOOL OF SCIENCE & TECHNOLOGY

DEPARTMENT OF MATERIALS SCIENCE

MADALENA ROSA CORREIA CALADO

Bachelor of Science in Micro and Nanotechnology Engineering

Pressure-Driven Resistive Pulse Nanopore Sensing for the Characterization of Extracellular Vesicles

MASTER OF SCIENCE IN MICRO AND NANOTECHNOLOGY ENGINEERING

NOVA University Lisbon

December, 2021

NOVA SCHOOL OF SCIENCE & TECHNOLOGY

DEPARTMENT OF MATERIALS SCIENCE

Pressure-Driven Resistive Pulse Nanopore Sensing for the Characterization of Extracellular Vesicles

MADALENA ROSA CORREIA CALADO

Bachelor of Science in Micro and Nanotechnology Engineering

Advisor: Dr. Alar Ainla, Staff Researcher, International Iberian Nanotechnology Laboratory, Braga, Portugal

Co-advisor: Dr. Hugo Águas, Associate Professor, NOVA School of Science and Technology | FCT NOVA

Examination Committee

Chair: Dr. Rodrigo Martins, Full professor in Materials Science Department, NOVA School of Science and Technology | FCT NOVA

Rapporteur: Dr. Victor Calero Martin, Research Fellow, International Iberian Nanotechnology Laboratory, Braga, Portugal

Member: Dr. Alar Ainla, Staff Researcher, International Iberian Nanotechnology Laboratory, Braga, Portugal

MASTER OF SCIENCE IN MICRO AND NANOTECHNOLOGY ENGINEERING

NOVA University Lisbon
December 2021

Pressure-Driven Resistive Pulse Nanopore Sensing for the Characterization of Extracellular Vesicles

Copyright © MADALENA ROSA CORREIA CALADO, NOVA School of Science and Technology, NOVA University Lisbon.

The NOVA School of Science and Technology and the NOVA University Lisbon have the right, perpetual and without geographical boundaries, to file and publish this dissertation through printed copies reproduced on paper or on digital form, or by any other means known or that may be invented, and to disseminate through scientific repositories and admit its copying and distribution for non-commercial, educational or research purposes, as long as credit is given to the author and editor.

"*You, the people, have the power to make this life free and beautiful, to make this life a wonderful adventure.*"
Charlie Chaplin, The Great Dictator (1940)

Acknowledgments

Firstly, I would like to thank everyone at INL that made this possible, especially Lorena Diéguez. It was an honor to be part of the Medical Devices group and get to know the people from the IMiNa and Food Processing groups. Loved our inter-group lunch meetings. Thank you to Claudia and Paulina for helping with the biological experiments. Also, thank you to Victor Calero. Your advice was fundamental.

It was truly an honor and a pleasure to have the opportunity of learning from Alar. There's a reason why he is everyone's go-to guy at INL. Thank you, Alar, for always being there for us. Thank you for the endless encouragement. We had many challenging moments during this time, but at least we knew we could count on you. I will miss cookie time. Thank you!

To everyone at ICVS: Patricia, Susana, Fernanda, and Jacinto, a big thank you! Without your help, this thesis wouldn't exist (literally). Thank you for sharing your knowledge with me.

To Professor Hugo, thank you for always being so helpful these last five years.

À Dona Rosalina, que há anos, mas especialmente nos últimos 5 anos, foi um grande apoio. Obrigada por me ouvir e me fazer a cama.

Ao maestro Miguel Madaleno, obrigada por formares a Orquestra Nova de Guitarras, à qual dei muito de mim, mas que me deu ainda mais de volta. Ajudaste a ser quem sou hoje.

A toda a gente do interquartos: Joana, Maria, Leonor, Bia, Duarte, Maggie, Gonçalo, André e Vitória, obrigada. Tem sido um prazer ver vos crescer.

To my Greek people: Elias, Jonas, Michi, Daniela, and Artur, you changed me forever, and I'm grateful for the time we had together. You all gave me the sun.

Ao meu companheiro nesta grande aventura no INL, ao Dani, um grande, grande obrigada. Sei que fui difícil de aturar depois de me ter tornado numa bola de stress. ATREIDES!

É impossível fazer um curso sozinho, tenho muito que agradecer aos my dudes: pokeyuri, Rui, Russo, Freire, Sérgio e Caril. Sem vocês muitos trabalhos teriam ficado por fazer. Obrigada.

Ao siligang, obrigada por me apoiarem sempre! Valorizo imenso a amizade que temos.

Aos meus bros Victor e Dias, um mega thank you. Nunca tenho histórias para contar, mas ao menos agora posso dizer que tenho uma tese. Vocês são fixes.

Lastly, and for sure the most important part of not only this thesis but also the last 5 years (and more), my family.

À avó Rosa e ao avô António, obrigada por me fazerem quem sou. Tenho saudades do arroz, das cantigas e de comer bolachas às escondidas. Espero que vos tenha deixado orgulhosos.

À Familia Grande Acima da Média: Jaquim, Altina, tia Maria Manuel, tio Jorge, Có, tia Paula, tio Zé, Mé, Sofas e Bia, obrigada! Sem vocês não teria conseguido. Tenho muita sorte em ter vos como família. Esta vitória também é vossa.

.

Abstract

Extracellular Vesicles (EVs) are highly involved in several biological processes within the human body. However, their involvement is not exclusive to conventional bodily functions since these vesicles can promote the spread and development of diseases due to their role in cell-to-cell communications. Thus, EVs have become serious biomarker candidates for the detection of pathological agents. Despite this, the current methods used to isolate and characterize EVs are often laborious and involve bulky laboratory instruments, hindering their routine use in healthcare. Therefore, developing new techniques to characterize them properly is of great interest.

To tackle this problem, we studied the combination of Resistive-Pulse Sensing with pressure-driven flow in two different nanopores – one formed from glass capillaries and another integrated into microfluidic chips. First, we characterized the transport using model particles, which generated current spikes when moving through the pore. These experiments were followed by using biological samples, such as human serum and purified EVs.

The results show that particle size strongly influences the current spike amplitude and width. Furthermore, it is possible to link relative current shift with the expected particle diameter, while frequency relates to particle concentration. By analyzing the relative current shift, we identified different population sizes in the complex biological samples.

This work extends the knowledge on particle detection and sizing techniques but is also helpful to understand the possibilities of using Resistive Pulse Sensing in the analysis of EVs.

Keywords: microfluidics, extracellular vesicles, pressure-driven flow, nanoparticles, resistive-pulse sensing.

Resumo

As Vesiculas Extracelulares (EVs) estão envolvidas em diversos processos biológicos do corpo humano. No entanto, devido ao papel destas vesiculas na comunicação entre células, este envolvimento não é exclusivo às funções corporais convencionais, uma vez que podem promover a disseminação de doenças. Assim, o interesse para usar as EVs como biomarcadores de agentes patológicos tem vindo a crescer. Apesar disto, os métodos atualmente implementados para isolar e caracterizar EVs são, muitas vezes, trabalhosos e envolvem equipamentos de laboratório volumosos, dificultando a sua implementação no típico contexto hospitalar. Assim sendo, existe um grande interesse em desenvolver novas técnicas capazes de as caracterizar adequadamente.

Para combater este problema, estudámos a combinação de Deteção de Pulso Resistivo com fluxo gerado por pressão em dois nanoporos diferentes – um formado a partir de capilares de vidro e outro integrado em dispositivos de microfluídica. Primeiro, caracterizámos o transporte usando partículas modelo, que ao atravessarem o poro geram picos de corrente. Estes testes foram seguidos pela análise de amostras biológicas, como sérum humano e EVs purificadas.

Os resultados mostram que o tamanho da partícula influencia fortemente a amplitude e a largura do pico de corrente. Além disso, é possível relacionar a alteração relativa da corrente com o diâmetro esperado da partícula, enquanto a frequência está relacionada com a concentração das partículas. Ao analisar esta alteração relativa da corrente conseguimos identificar nas amostras biológicas a existência de populações com diferentes dimensões.

O presente projeto expande o conhecimento sobre técnicas de deteção e dimensionamento de partículas, sendo também útil para compreender as diferentes possibilidades de usar Deteção de Pulso Resistivo na análise de EVs.

Palavras-chave: microfluídica, vesiculas extracelulares, fluxo gerado por pressão, nanopartículas, Deteção de Pulso Resistivo.

Table of Contents

ACKNOWLEDGMENTS IX

ABSTRACT XI

RESUMO XIII

LIST OF FIGURES XVII

LIST OF TABLES XIX

ACRONYMS XXI

SYMBOLS XXIII

1 MOTIVATION AND OBJECTIVES 1

2 INTRODUCTION 3

2.1 Extracellular Vesicles 3

2.1.1 Isolation techniques 3
2.1.2 Characterization Techniques 4

2.2 Microfluidics 4

2.2.1 Electrical transport 5
2.2.2 Pressure-driven transport 6

2.3 Resistive-Pulse Sensing 7

3 MATERIALS AND METHODS 9

3.1 Nanopipette fabrication and characterization 9

3.2 Microfluidic device fabrication 9

3.3 Resistive-Pulse Sensing measurements 9

3.4 Nanoparticle and PBS solutions 10

3.4.1 Nanoparticle concentration 10
3.4.2 Dynamic Light Scattering 10

3.5 Biological Experiments 10

4 RESULTS AND DISCUSSION 11

4.1 Glass nanopipettes 11

4.1.1 Pipette Dimensions 11
4.1.2 Particle Detection 12
4.1.3 Summary 12

4.2 PDMS microfluidic chips 12

4.2.1 Theoretical calculations 15
4.2.2 Pressure Dependence 17
4.2.3 Device behaviors and measurements scenarios 18
4.2.4 Design Optimization 20
4.2.5 Pulse Shape Analysis 22

4.2.6 Concentration study 23
4.2.7 NP mixture study 25
4.2.8 Biological Experiments 27
4.2.8.1 Human Serum 27
4.2.8.2 Purified EVs 28
4.2.9 Patch-Clamp Amplifier vs. RPS Interface 29
5 CONCLUSIONS AND FUTURE PERSPECTIVES 31
6 REFERENCES 33
7 SUPPORTING INFORMATION 35
7.1 Nanopipette fabrication and characterization 35
7.1.1 Nanopipette pulling 35
7.1.2 Nanopipette characterization 36
7.2 Optical Microscope Images 37
7.3 Nanoparticle concentration conversion 37
7.4 Dynamic Light Scattering Results 38
7.5 Nanopipette Patch-Clamp schematic 38
7.6 Nanopipette Cone Resistance 38
7.7 Nanopipette Particle Detection Results 39
7.8 Examples of the categorized behaviors 41
7.9 Theoretical values and equations 45
7.9.1 Electrical Resistance 45
7.9.2 Relative Current Amplitude Shift 47
7.9.3 Nanoparticle diameter equation 47
7.9.4 Electrical transport 49
7.9.5 Hydrodynamic Resistance 49
7.10 Biological Experiments 51
7.10.1 Human Serum 51
7.10.2 Purified EVs 52
7.11 Patch-Clamp Amplifier vs. RPS Interface 53

List of figures

FIGURE 1 – SCHEMATIC OF ELECTRICAL DOUBLE LAYER. ADAPTED FROM [21]. 5
FIGURE 2 – SCHEMATIC OF [A] ELECTROOSMOTIC FLOW AND [B] PRESSURE-DRIVEN FLOW. 6
FIGURE 3 – THE SCHEMATIC ILLUSTRATION OF RESISTIVE-PULSE SENSING. THE MOVEMENT OF A PARTICLE GOING THROUGH A PORE CAN BE DIVIDED INTO 3 DIFFERENT MOMENTS. THESE WILL AFFECT THE CURRENT IN DIFFERENT WAYS, WHICH RESULTS IN A CURRENT SPIKE 7
FIGURE 4 – SCHEMATIC OF ZOOMED-IN GLASS NANOPIPETTE. 11
FIGURE 5 – SCHEMATIC OF PATCH-CLAMP SET-UP AND THE FABRICATED PDMS MICROCHIPS. EVERYTHING THAT WAS CONNECTED TO THE DEVICE DURING EXPERIMENTS IS ALSO REPRESENTED: PRESSURE CONTROLLER (BLUE), ELECTRODE (PINK), AND REFERENCE ELECTRODE (BLACK). 13
FIGURE 6 – SCHEMATIC OF THE PDMS CHIPS WITH DIFFERENT STRUCTURES: MACROCHANNELS (BLUE), MICROCHANNELS (GREEN), AND NANOCHANNEL (RED). THERE ARE THREE DIFFERENT TYPES OF NANOCHANNEL (SMOOTH, SINGLE, AND DOUBLE CONSTRICTION). 13
FIGURE 7 – SCHEMATIC OF THE RELATIONSHIP BETWEEN PORE GEOMETRY AND THE OBTAINED CURRENT SPIKES. IT IS ALSO HIGHLIGHTED, WHERE THE SPIKE PARAMETERS (WIDTH AND HEIGHT) ARE TAKEN. 14
FIGURE 8 – IDEAL DEVICE DATA AND BEHAVIOR: [A] RAW DATA, [B] SPIKE AMPLITUDE VS. PRESSURE APPLIED, [C] SPIKE WIDTH VS. PRESSURE APPLIED, AND [D] PARTICLE VELOCITY IN FUNCTION OF THE PRESSURE APPLIED. DATA SET OBTAINED WITH DESIGN 5 AND 500 NM NPS. 18
FIGURE 9 – [A] RAW SIGNAL OF DOUBLE SPIKES MEASUREMENTS IN DESIGN 12 WITH 500 NM NPS, AND APPLYING 75 MBAR, AND CORRESPONDING [B] LATENCY HISTOGRAM. IN THE LATENCY HISTOGRAM IS REPRESENTED THE EXPONENTIAL DECAY OF POISSON PROCESS (GREEN) AND A GAUSSIAN DISTRIBUTION (PURPLE). 23
FIGURE 10 – GRAPHS OF SPIKE FREQUENCY VS. THE PARTICLE CONCENTRATION, USING LOG-LOG REGRESSIONS. FOR [A], [B] SMOOTH, [C] SINGLE, AND [D] DOUBLE CONSTRICTION CHANNELS. THE SPIKES WERE COUNTED IN THE 100 OR 150 MBAR REGION OF THE MEASUREMENTS. 24
FIGURE 11 – [A] RAW DATA WITH THE REGISTERED SPIKES MARKED IN RED AND THE TWO POPULATIONS IDENTIFIED WITH A DASHED LINE (NOT ACCURATE, JUST REPRESENTATIVE). [B] HISTOGRAM OF THE EXPECTED AMPLITUDE SHIFT. [C] HISTOGRAM OF THE EXPECTED NP DIAMETER OF THE NPS MIXED TOGETHER. THE IDENTIFIED POPULATIONS ARE MARKED BY BLACK ARROWS. ONLY 100 AND 150 MBAR WERE APPLIED DURING THIS MEASUREMENT. 26
FIGURE 12 – HISTOGRAMS OF THE EXPECTED NP DIAMETER OF THE HUMAN SERUM SAMPLE IN [A] DESIGN 5 FOR 100 AND 150 MBAR, AND [B] DESIGN 2 WITH ONLY APPLYING 150 MBAR. THE IDENTIFIED POPULATIONS ARE MARKED BY BLACK ARROWS. 28
FIGURE 13 – HISTOGRAMS OF THE EXPECTED NP DIAMETER OF THE PURIFIED EVS SAMPLE IN [A] DESIGN 5 AND [B] DESIGN 2. THE IDENTIFIED POPULATIONS ARE MARKED BY BLACK ARROWS. THE SPIKES IN DESIGN 5 WERE REGISTERED WITH 150 MBAR, WHILE IN DESIGN 2 IT WAS APPLIED 100 AND 150 MBAR. 29
FIGURE 14 – STEP BY STEP IMAGES OF THE NANOPIPETTE PULLING PROCESS: (A) THE PIPETTE PULLER MACHINE, (B) GLASS CAPILLARY GOING THROUGH THE FILAMENT, (C) THE HEATING OF THE CAPILLARY, AND (D) THE TRANSFORMATION OF THE GLASS CAPILLARY INTO TWO PIPETTES. 35
FIGURE 15 – SEM IMAGES OF THE PULLED NANOPIPETTES: (A) PIPETTE A, (B) PIPETTE B, AND (C) PIPETTE C. MARKED IN YELLOW IS THE PLACE WHERE THE ID MEASUREMENTS WERE TAKEN. 36
FIGURE 16 – IMAGES CAPTURED WITH AN OPTICAL MICROSCOPE OF [A] DESIGN 7 AND [B] DESIGN 12. 37
FIGURE 17 – PATCH-CLAMP SCHEMATIC OF EXPERIMENTS ON GLASS NANOPIPETTES. ADAPTED FROM "PATCH-CLAMP RECORDING PRINCIPLE", BY BIORENDER.COM (2021). RETRIEVED FROM HTTPS://APP.BIORENDER.COM/BIORENDER-TEMPLATES 38
FIGURE 18 – BASELINE CURRENT OVER TIME FOR EXAMPLE 1. 39
FIGURE 19 – CURRENT GRAPHS FOR EXAMPLE 2. THE DETECTED SPIKES ARE MARKED IN RED. 40

FIGURE 20 – WORKING DEVICE GRAPHS FOR THE IDENTIFIED BEHAVIORS: [A] ONE DATA POINT ONLY, ALL THE SUDDEN CLOGGING VARIATIONS ([B], [C], [D]), [E] FEW SPIKES BUT OBEYS THE FREQUENCY RULE, [F] UNSTABLE BASELINE. THE DATA SETS FROM [A] TO [E] HAVE THREE GRAPHS: RAW DATA, SPIKE AMPLITUDE VS. PRESSURE APPLIED, AND SPIKE WIDTH VS. PRESSURE APPLIED. THE LAST DATA SET [F] HAS THE RAW DATA AND THE HISTOGRAM OF THE RELATIVE AMPLITUDE SHIFT. THE SPIKES REGISTERED ARE MARKED IN RED IN THE RAW DATA GRAPH. 43
FIGURE 21 – RAW DATA OF THE NON-WORKING DEVICES FOR THE IDENTIFIED BEHAVIORS: [A] NO SPIKES, [B] MANY BUBBLES GOING THROUGH THE PORE AFTER A FEW SPIKES AND CLOGGING, AND [C] TOO MUCH NOISE. 44
FIGURE 22 – RAW DATA AND HISTOGRAMS OF THE RELATIVE AMPLITUDE SHIFT OF THE HUMAN SERUM SAMPLE IN [A] DESIGN 5 AND [B] DESIGN 2. 51
FIGURE 23 – SIZE DISTRIBUTION OF THE PURIFIED EVS SAMPLE, OBTAINED BY ULTRACENTRIFUGATION. THIS WAS PROVIDED BY INL COLLABORATORS. 52
FIGURE 24 – RAW DATA AND HISTOGRAMS OF THE RELATIVE AMPLITUDE SHIFT OF THE PURIFIED EVS SAMPLE IN [A] DESIGN 5 AND [B] DESIGN 2. 52
FIGURE 25 – ZOOMED IN SPIKES FROM THE INL-MADE RPS INTERFACE (RED) AND PATCH-CLAMP AMPLIFIER (BLUE), FOR [A] A SMOOTH CHANNEL, [B] A SINGLE CONSTRICTION, AND [C] A DOUBLE CONSTRICTION CHIP. 53

List of Tables

Table 1 – Classification of Extracellular Vesicles by the size and origin. 3
Table 2 – List and concentration of nanoparticle solutions used in experiments. 10
Table 3 – Inner diameter of the nanopipettes produced from Recipe 1 and its corresponding resistance measured by Patch-Clamp. 11
Table 4 – Parameters used in two tests and the resistance measured by patch-clamp. 12
Table 5 – Chip designs and their dimensions. It is also represented, which NPs were used with each chip design. 14
Table 6 – Total theoretical resistance of the channels and the expected relative amplitude shift caused by the NPs in each design. 15
Table 7 –Relative Amplitude shift and the corresponding NP diameter for each NP in different designs. 15
Table 8 – Field strength in the pore, mobility, and velocity (electroosmotic and electrophoretic) for each design on low salt solutions. 16
Table 9 – The hydrodynamic resistance of the nanochannel and the corresponding flow rate for each design. 16
Table 10 – Hydrodynamic velocity for each design depending on pressure applied. 17
Table 11 – The success rate for spike detection obtained for each NP, device design and solution combination. 20
Table 12 – Relative Spike Amplitude and Expected NP diameter analysis for the combinations that passed the first test. The measured relative amplitude shift was taken at 100 mbar. 21
Table 13 – Average spike width at 100 mbar. Comparison between the velocity from experimental data and the hydrodynamic velocity obtained in section 4.2.1. 22
Table 14 – Slope and intercept value of the linear regression for each channel type. 24
Table 15 – Expected spike frequency (Hz) depending on solution concentration for each channel type. 25
Table 16 – Expected relative current amplitude shift and NP diameter for each particle in Design 5. The associated relative error of the approximation was also calculated. 26
Table 17 – Serum fraction present in the solutions used with the corresponding total protein concentration. 27
Table 18 – Parameters used that got the most relevant results. 35
Table 19 – Average of the measured Zeta Potential for each NP. 38
Table 20 – Specific parameter values obtained from the analyzes of the spikes. 40
Table 21 – Resistance of the macro and microchannels for low and high salt solutions. 45
Table 22 – Dimensions of all the nanochannel components. 46
Table 23 – Resistance values for each component of the nanochannel and the total resistance. 46
Table 24 – Relative current amplitude shift for each design according to which particle is present in the pore. 47
Table 25 – Expected NP diameter calculated from the relative current shift. 48
Table 26 – Field strength and electroosmotic velocity for all designs according to salt concentration. 49
Table 27 – Hydrodynamic resistance of all the nanochannel components for each design. 50
Table 28 – Parameter comparison between the RPS interface and Patch-Clamp the different channel types. 54
Table 29 – Comparison between Patch-Clamp and In-house made RPS Interface success rate. 55

Acronyms

EVs	Extracellular Vesicles
NP	Nanoparticle
SEC	Size exclusion chromatography
PDMS	Polydimethylsiloxane
DLS	Dynamic Light Scattering
NTA	Nanoparticle Tracking Analysis
EDL	Electrical Double Layer
EP	Electrophoresis
EOF	Electroosmotic Flow
RPS	Resistive-pulse sensing
sPDMS	Soft PDMS
hPDMS	Hard PDMS
PBS	Phosphate Buffered Saline
HS	High salt concentration
LS	Low salt concentration
ID	Inner Diameter
OD	Outer Diameter

Symbols

ϕ	Electrical potential of surface
e	Euler's number
λ_D	Debye length
ε_0	Vacuum permittivity
ε_r	Dielectric permittivity
k_B	Boltzmann's constant
T	Temperature
n_0	Density of ions
q	Ionic charge
ζ	Zeta potential
η	Dynamic viscosity of the fluid
μ_{EOF}	Electroosmotic mobility
v_{EOF}	Electroosmotic velocity
μ_{EF}	Electrophoretic mobility
v_{EF}	Electrophoretic velocity
E	Electric field strength
Q	Flow rate
R_{hyd}	Hydrodynamic resistance
P	Pressure
v_{hyd}	Hydrodynamic velocity
ρ	Resistivity
σ	Conductivity
L	Length
W	Width
H	Height
r	Radius of cylinder section of a pipette
L_P	Length of the nanopore
W_P	Width of the nanopore
H_P	Height of the nanopore
L_S	Length of the pore separation
R_{total}	Total theoretical resistance
I_{rel}	Relative current amplitude shift
R_{PP}	Pore resistance in the presence of particle
d	Particle diameter
$R_{hydNANO}$	Hydrodynamic resistance in the nanochannel
C	Solution concentration
ρ_d	Particle density
R_{nano}	Resistance of the nanochannel
R_{micro}	Resistance of the microchannel
R_{macro}	Resistance of the macrochannel
L_A	Length of part A of the microchannel
W_A	Width of part A of the microchannel

L_B	Length of part B of the microchannel
W_B	Width of part B of the microchannel
R_P	Resistance of the pore
R_C	Connector resistance
R_{PC}	Pre-connector resistance
R_S	Separation resistance
W_C	Width of the connector
H_C	Height of the connector
L_{PC}	Length of the pre-connector
W_{PC}	Width of the pre-connector
H_{PC}	Height of the pre-connector
L_S	Length of the separation
W_S	Width of the separation
H_S	Height of the separation
R_{TP}	Total resistance of the system in the presence of a particle
J	Current density
I	Current across the pore
A	Cross sectional area of the pore
V	Voltage applied
h	Height of the channel in which the R_{hyd} is being calculated
w	Width of the channel in which the R_{hyd} is being calculated
R_{hydP}	Hydrodynamic resistance of the pore
R_{hydC}	Hydrodynamic resistance of the connector
R_{hydPC}	Hydrodynamic resistance the pre-connector
R_{hydS}	Hydrodynamic resistance of the separation

1 Motivation and Objectives

Micro- and nanoparticles play a crucial role in many biological processes. A few examples of these essential particles are synaptic vesicles, small bacteria, viruses, protein complexes, and importantly Extracellular Vesicles.

Extracellular Vesicles (EVs) can be found on almost all body fluids, as these small vesicles are involved in various processes of the human body. They can transport proteins, nucleic acids, and lipids from cell-to-cell. The EVs present in the bloodstream are interesting for many potential applications [1]. One of the most relevant applications for these small vesicles would be their use as cancer biomarkers. Therefore, it makes the isolation and analysis of such particles highly relevant for clinical diagnostics and cancer research [2].

Microfluidics is a technology field where liquids are manipulated in channels with micrometer dimensions, making it attractive to characterize small particles. It differs from its larger relative, millifluidics, by channel dimensions and the different physical behaviors specific to this scale, which will be further studied in this thesis.

This project aims to characterize the transport of nanoparticles for the application of EVs analysis through nanopores formed either from glass capillaries or integrated into microfluidic chips by applying controlled pressure. Specific objectives of the project were the following:

- Obtaining and studying nanoparticle (NP) signals with resistive pulse sensing (RPS) using different channel geometries, NP dimensions, and buffer compositions.
- Study pressure dependence of these signals.
- Study concentration dependence and detection limit.
- Demonstrating RPS with biologically relevant samples (human serum and purified EVs).

In terms of structures, this work will be divided into four main sections: the introduction, where the essential background will be given; the materials and methods part, where the experimental conditions used will be described; the results and discussion section, where the obtained data will be presented and explained; and finally, conclusion of this thesis.

2 Introduction

2.1 Extracellular Vesicles

Extracellular Vesicles are made of a phospholipid bilayer and are released by most cells in the body, and can be found in many biological fluids, such as blood plasma and serum, saliva, and urine. These vesicles are responsible for mediating cell-to-cell interactions, as they carry proteins, lipids, and nucleic acids through the lipid membrane to the outside of the cell. EVs are commonly divided into subtypes based on their size and formation process (Table 1) [1], [3]–[5].

Table 1 – Classification of Extracellular Vesicles by the size and origin.

EV type	Size (nm) [3]	Origin
Exosome	30 - 120	In the endocytic pathway, the inward budding of the plasma membrane forms early endosomes. These mature into multivesicular bodies that fuse with the membrane and release its contents, exosomes, to the extracellular medium [3], [4].
Microvesicles	120 - 1000	Result from the outward budding of the plasma membrane [3].
Apoptotic Bodies	5000	Formed during cell apoptosis from collapsing plasma membrane [3].

However, EVs can also be involved in spreading and developing diseases due to their crucial role in cell communication. They can spread viral infections quicker as they enhance the infectivity of viruses by transporting multiple viral particles and genomes to new cells [6]. Moreover, EVs can also induce neurogenerative disorders. EVs that derive from brain cells can carry proteins prone to aggregation. Many neurodegenerative diseases, such as Alzheimer's, Parkinson's, and Huntington's diseases, are characterized by the accumulation of aggregated proteins in cells [7]. Furthermore, EVs are also highly involved in tumor development. As their function is to interact with other cells, it has many consequences, when tumor-derived EVs are incorporated by heathy cells, as this can improve tumor growth and invasion, and the development of metastasis [3], [8].

To study EVs it is essential to isolate and characterize them. The most common and emerging techniques for the isolation and characterization of EVs are described in the following sections.

2.1.1 Isolation techniques

For the isolation of extracellular vesicles, many approaches have been developed from more conventional methods to innovative microfluidic technologies.

These conventional techniques include differential ultracentrifugation that isolates EVs by applying a high centrifugation force. Even though it is the most common method, it has low throughput, is time-consuming, and has low specificity, as other particles can also be isolated together [9], [10]. Another method is Size Exclusion Chromatography (SEC) which, according to the different sizes of the particles passing through a porous matrix, separates them, and as EVs are bigger, they elute first. Even though this method has a high yield, it isolates not desired low-density particles, and small EVs may be lost [9]. Another example is immunoaffinity isolation. Unlike the other methods described here, based on the physical characteristics of EVs, immunoaffinity isolation relies on the proteins expressed on their surface, enabling more EV-specific isolation. In this method, the EVs are recognized by an antibody coupled with "beads", which allows their separation. However, not all EVs are separated, as there has not been found an antibody that binds to all subtypes of EVs

[11]. Some conventional methods need specialized equipment that can be expensive. The samples resulting from these isolation methods are often not pure, have a low yield, or the integrity of the EVs is compromised during isolation. Due to these recurring challenges, there is a great motivation to shift towards microfluidic devices to isolate EVs instead.

Many different techniques using microfluidic chips have been developed to isolate EVs. Often these isolation techniques are based on the presence of specific surface markers, or the size and density of the EVs. Microfluidics based on immunoaffinity uses antibodies to target specific surface markers present on EVs. The walls of these microfluidic devices are modified with antibodies. This technique can efficiently capture EVs with high specificity. However, it is strongly dependent on previous knowledge about the surface antigens present, leading to capturing only a subpopulation of all the EVs.

On the other hand, microfluidics based on membrane filtration is specific to the size of EVs. Double-filtration microfluidic systems trap cells and protein aggregates on the first filter and EVs on the second filter, separating them from any remaining smaller proteins. This technique has high throughput and yield, when compared to a conventional method such as ultracentrifugation. Another filtration system uses silicon micropillars in the microfluidic channels to sort EVs and separate them from bigger and smaller particles. These methods sort EVs with high purity and integrity, but the system can become saturated with higher sample volume [9], [12].

2.1.2 Characterization Techniques

The characterization of samples of EVs in labs still involves bulky equipment and laborious work. Thus, there is a need to develop miniaturized systems, that can analyze these samples, while requiring smaller sample volumes, are portable and reusable [12]. The integration of EV characterization in microfluidic chips would expand the potential application of EVs as biomarkers, promoting their routine use in healthcare.

There are many techniques available to characterize EVs. In the case of TEM and SEM, these techniques allow us to know the morphology and size of the EVs. However, these are costly techniques that require complex sample preparation and extensive operating knowledge. The analysis of suspended particles in liquids is still a challenge. AFM allows getting information about the topography of EVs when they are attached to a substrate by antibodies, both in air and liquid modes [13]. However, their characterization is time consuming, and there is also the risk of deformation by the cantilever tip. DLS measurements are perfect for determining particle size distribution in a liquid, but it is challenging to characterize individual particles. NTA has the same working principle as DLS but can characterize individual EVs. Both techniques are very quick and do not need complex sample preparation, but both are greatly hindered by polydisperse samples and have limited resolution. Although these techniques are well suited for estimating the size of the EVs, they are not specific for these, as other contents of the sample, like protein aggregates can scatter light, which leads to concentration overestimation. Furthermore, in polydisperse samples, the bigger EVs will scatter more light even in lower concentrations and “hide” the less intense light scattered by smaller EVs, which will move the detected size range to larger diameters. A filtration of the sample beforehand could be a solution for this problem [12], [14], [15].

As shown here, there are already many methods able to analyze EVs. However, most of them still have limitations. Therefore, there is need to develop a more accurate technique, that could characterize single EVs, which directed the choice of method in this work to Resistive Pulse Sensing. This technique will be further explained later in this section.

2.2 Microfluidics

Liquids behave differently, when in channels with different dimensions. Millifluidics, microfluidics, and

nanofluidics study the transport of liquids confined to devices with structures in the millimeter, micrometer, and nanometer scale, respectively. The smaller the scale, the more dominant surface and chemistry effects become. In terms of fabrication methods, in research, microfluidic devices are commonly fabricated using soft lithography. In this method, typically, a master substrate (e.g., silicon wafer) is patterned using other lithography techniques. The pattern is replicated by polydimethylsiloxane (PDMS), which is bonded to a glass substrate [16].

Microfluidic devices have a wide variety of applications: particle separation, single-cell analysis, organ on a chip, point-of-care diagnostics [16], drug delivery [17], cancer detection [18], [19], and the identification of foodborne pathogens [20], are just a few examples of applications of microfluidic systems.

2.2.1 Electrical transport

As mentioned previously, the surface effects become more dominant in microfluidics as the surface-to-volume ratio increases. Therefore, the flow of the fluid becomes dependent on the surface chemistry.

When a surface gets in contact with an electrolyte, it becomes charged. Most of the materials used to make microchannels (e.g., glass or many polymers) become negatively charged at neutral pH. As a result, it will attract ions of opposite charge and repel ions of the same charge, creating an Electrical Double Layer (EDL) at the interface. The EDL has two different regions: the Stern layer, closest to the interface and made of compact counter-ions, and the diffusion layer, the outer region of the EDL, where there is a surplus of counter-ions and only a few co-ions, which are mobile (Figure 1) [21], [22]. When immersed in an electrolyte, the same happens to particles, as there is an EDL formed at their surface. This allows for the characterization of the particles regarding their zeta potential and electrophoretic mobility.

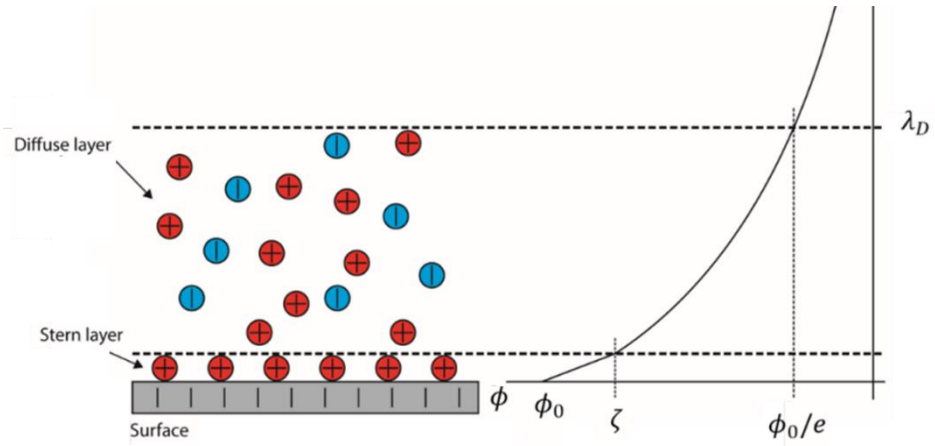

Figure 1 – Schematic of Electrical Double Layer. Adapted from [21].

The thickness of the EDL can be estimated by calculating the Debye length, which represents the distance at which the electrical potential of the surface (ϕ) decreases to $1/e$ of its initial value (e is Euler's number) [21]. If assuming a symmetric monovalent electrolyte such as NaCl, the Debye length (λ_D) equation can be calculated as follows:

$$\lambda_D = \sqrt{\frac{\varepsilon_0 \varepsilon_r k_B T}{2 n_0 q^2}}\ (m) \qquad (1)$$

where n_0 is the density of ions, q is the ionic charge, ε_0 is the vacuum permittivity, ε_r the dielectric permittivity, k_B is Boltzmann's constant and T the temperature. The Debye length strongly depends on the electrolyte concentration. A concentrated electrolyte has a smaller Debye length, unlike a diluted electrolyte that has a larger Debye length, due to the lesser screening of the charge.

Figure 1 also shows the zeta potential (ζ), which represents the electrical potential at the boundary

between the Stern and diffusion layer relative to the bulk solution. The zeta potential is an important physical property of any particle suspension, as it indicates the stability of the system. It is desired that the NPs have a large (negative or positive) zeta potential, as this means that the particles will repeal each other and not create aggregates. This potential is dependent on the pH, conductivity, and ionic concentration of the sample [23].

When particles are suspended in an electrolyte and an electric field is applied, this gives rise to electrokinetic phenomena, such as Electrophoresis. Electrophoresis (EP) describes the movement of a particle in a fluid along the electric field, which is due to the interaction of the electrical field with the ions of the EDL surrounding the particle [21], [24]. The velocity of the particles is proportional to the electrical field applied. This relationship is represented by the electrophoretic mobility, the proportionality constant. In a situation, where the diameter of the particle is much bigger than the thickness of the EDL ($d/\lambda_D >> 1$), the electrophoretic mobility is given by:

$$\mu_{EP} = \frac{\varepsilon_r \varepsilon_0 \zeta}{\eta} \ (m^2 / V \cdot s) \tag{2}$$

where η is the dynamic viscosity.

When an electrical potential is applied along microfluidic channels the positive counter ions close to the channel walls are attracted by the negative electrode and start flowing towards it, giving rise to another electrokinetic phenomenon called Electroosmosis. The corresponding liquid movement is called Electroosmotic flow (EOF). Inside the channels of the microfluidic device, the EOF is constant and has a plug flow profile (Figure 2A) [21]. The velocity of the EOF is given by:

$$v_{EOF} = \mu_{EOF} E \ (m/s) \tag{3}$$

where μ_{EOF} is the electroosmotic mobility, which is the symmetric of μ_{EP} as they act in opposite directions, and E is the electric field strength.

2.2.2 Pressure-driven transport

The phenomena mentioned above led to unique transport characteristics in micro- and nanofluidic devices. However, electrical transport is not the only way to get particles to move. It is also possible to do it with pressure-driven flow.

Pressure-driven flow generates a parabolic flow, unlike EOF (Figure 2B). Its velocity profile maxes at the center of the channel and is zero at the channel walls, meaning there is almost no movement of fluid close to the surfaces. In the case of lower salt concentrations and small channels, the EDL can extend to the center of the channel, as screening is weaker. This extension matches the region where the fluid velocity is the highest. This causes a streaming electrical current and voltage induced by pressure-driven flow, which is higher for lower salt concentrations [25].

To analyze pressure driven-flow in the network of channels in microfluidic devices, the same framework of rules similar to Kirchhoff and Ohm's laws can be used by replacing voltage, current and electrical resistance with pressure, flow rate and hydrodynamic resistance, respectively [26].

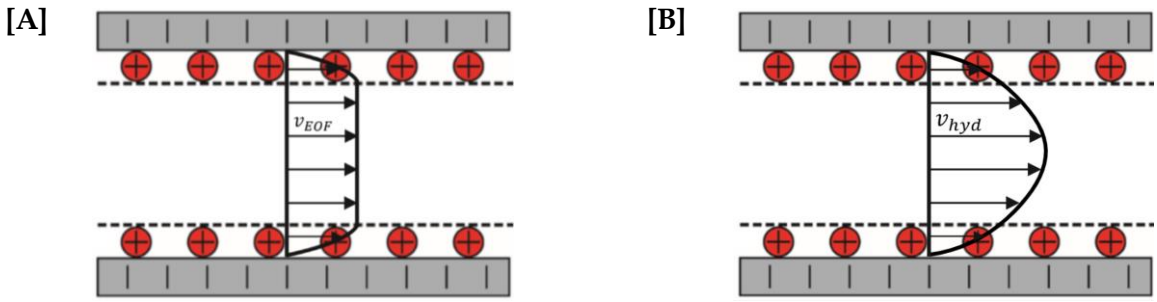

Figure 2 – Schematic of [A] Electroosmotic Flow and [B] Pressure-driven flow.

According to the Hagen-Poiseuille law, it is possible to relate the pressure applied (P) with the hydrodynamic resistance (R_{hyd}), obtaining the flow rate (Q) of the fluid [26]. This relation is given by:

$$Q = \frac{P}{R_{hyd}} \ (m^3/s) \tag{4}$$

For instance, as in electronics, the hydrodynamic resistance strongly depends on the geometry of the channels, and different channel geometries have different equations to describe their resistance [26]. Moreover, it is important to characterize the velocity of the particles passing through the channel. The velocity calculation can be extremely complex, while the average hydrodynamic velocity can be obtained using the relation between the flow rate and the cross sectional area of the channel, which is given by:

$$v_{hyd} = \frac{Q}{cross\ sectional\ area} \ (m/s) \tag{5}$$

2.3 Resistive-Pulse Sensing

A technique able to count blood cells based on electrical principles was invented in 1940 by W. Coulter, this technique is called Coulter Counter [27]. Since then, it evolved and gave rise to a new method called Resistive-Pulse Sensing (RPS). This method is label-free, does not damage the particles to be detected, and has a fast processing time. The equipment needed is simple and consists of having two volumes containing an electrolyte solution connected by a small pore. When a potential is applied between electrodes in each of the volumes, current is generated. The electrolyte solution has small particles suspended, and when one of these particles passes through the pore, from one volume to the other, there is an increase in pore resistance, resulting in a drop in current (spike) (Figure 3) [28].

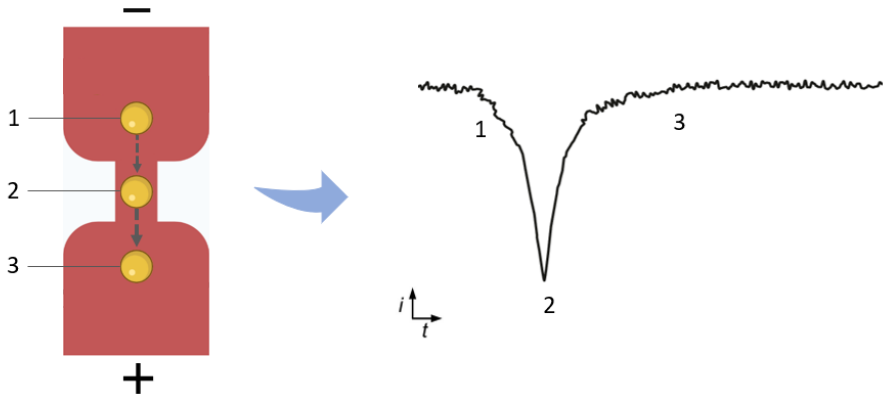

Figure 3 – The schematic illustration of Resistive-Pulse Sensing. The movement of a particle going through a pore can be divided into 3 different moments. These will affect the current in different ways, which results in a current spike

Often spike characteristics can give information regarding the particle size and the pore geometry. The relationship between particle size and the geometry of the pore dictates the amplitude of the spike. For pores smaller in width, pulse amplitudes are larger as there are larger changes in conductance. When pores are longer, the spikes are wider as the particles have a longer translocation time, when compared to shorter pores. However, for the same pore, if two different-sized particles pass through it, the larger particle will make a spike with a higher amplitude, as bigger volumes will block more current [28], [29].

The initial Coulter Counter did not stop evolving, as RPS is used in many types of devices, such as pipettes [14], membranes or conical pores, and for different purposes. The Coulter technique started by counting cells, but now RPS is even used for DNA sequencing [30], and to characterize viruses and proteins [31].

We believe, the combination of microfluidic resistive pulse sensing with pressure-driven flow is also a promising technique for EV characterization, making the analysis process, potentially more accurate, easier and faster than many typical characterization techniques used previously.

3 Materials and Methods

3.1 Nanopipette fabrication and characterization

The glass nanopipettes were produced from Borosilicate glass capillaries (GB150F-8P, Science Products). These capillaries were pulled using a P-97 Flaming/Brown Micropipette Puller (Sutter Instrument Company). Further information about the fabrication and characterization of glass nanopipettes can be found in section 7.1 of the Supporting Information.

3.2 Microfluidic device fabrication

The microfluidic devices were made of polydimethylsiloxane (PDMS). The fabrication process consists of the master mold fabrication, the PDMS replica molding, and the assembling of the chips.

The master mold was fabricated by the INL Cleanroom facility team in a 3-layer structure, containing both micro and nanochannels. Firstly, SiO_2 was patterned by e-beam lithography to produce nanochannels with 0.5-1 µm in height. Then, using two different formulations of SU-8, the supply channels with 15 µm in height and macrochannels with ~100 nm in height, using conventional photolithography methods. To ensure that the PDMS would not stick to the hydroxyl groups on the surface, the finished master mold went through a silanization process. It was placed in a vacuum desiccator with a drop of fluorocarbon silane.

Two types of PDMS were used to fabricate the PDMS chips: soft PDMS (sPDMS) (SYLGARD™ 184 Silicone Elastomer Kit, Dow) and hard PDMS (hPDMS) (GELEST®, Cymit Química). To make the sPDMS, the curing agent and the elastomer base were mixed in a 1:10 ratio. On the other hand, the elastomer base and the crosslinker of the hPDMS were mixed in a 1:1 ratio. Both were put in a vacuum desiccator to remove the bubbles in the mixtures.

To avoid the collapsing of the nanochannels, the hPDMS and the sPDMS were combined in a 1:1 ratio. After putting the smallest amount in the area around the nanochannel, the wafer was placed in the oven at 65ºC for half an hour, after which the sPDMS mixture was poured on top, making the layer 0,5 cm thick. The wafer was again placed in the oven at the same temperature for at least 12 hours.

Lastly, the chips were assembled. To start the process, the PDMS was peeled off from the master mold. The peel-off needs to be done carefully and slowly not to damage the nanochannels. Then, the PDMS layer was cut to separate the different designs, and 3 mm holes were punched to create the wells.

After that, the PDMS chips were bonded to a glass substrate using a Plasma Cleaner (PDC-002-CE, Harrick Plasma). These were placed in the oven at 65 ºC for 2 minutes. Then, to make sure the inside walls of the channels would become hydrophilic, droplets of Pluronic F-127 (Sigma Aldrich) 0.1% (w/v) solution were inserted into the wells making sure the solution passed the nanochannels.

As a final step of this fabrication process, the chips were inspected using an optical microscope (10x lens, Nikon Eclipse L200N). Images taken with this microscope are in section 7.2 of the Supporting Information. Then, these were labeled, covered by tape, and stored in the fridge.

3.3 Resistive-Pulse Sensing measurements

Two different measuring equipment were used in this thesis: Patch-clamp amplifier and an In-house made RPS interface. Patch-Clamp amplifier was used to acquire data from experiments on glass nanopipettes and PDMS chips. The signal was amplified by a MultiClamp 700B (Molecular Devices), low-pass filtered at 1 kHz, digitized with a 20 kHz sample rate (Digidata1440A, Molecular Devices). The data was recorded on a computer using Clampex software. In the case of the In-house Interface, it was only used for experiments on

PDMS chips. This interface has a bias voltage range of -5V to +5V. A gain of 40M was always used in our experiments, given a current raging from –125 to +125 nA.

Besides applying voltage, in all experiments, pressure was also applied. A computer-controlled pressure supply was used (FLUIKA PG500, Fluika OÜ), with a range of 0 to 500 mbar.

The data acquired from the RPS interface and Patch-Clamp Amplifier were analyzed using MATLAB scripts written purposely for this project.

3.4 Nanoparticle and PBS solutions

We used Phosphate Buffered Saline (PBS) as the electrolyte. The PBS solutions were made from 1X PBS Powder Concentrate, with 81% NaCl (Fisher Bioreagents BP661-10). The low salt PBS solution (LS) had a 137 mM NaCl concentration, and the high salt PBS solution (HS) had a 1 M NaCl concentration. The pH of the solutions was 7,654.

Three different nanoparticles (polystyrene beads) were used in this thesis, and their diameter and solution concentration are displayed in Table 2. The solutions concentration was converted into particles/mL using the equation in section 7.3 of the Supporting Information. The 252 nm (PS-R-KM239, microParticles GmbH) and 500 nm (F8812, Invitrogen) beads were purchased, while the 230 nm ones were provided by INL researchers using the method described in [32]. For each NP size, 8 solutions were made, combining the NP concentration with either high or low salt concentration.

Table 2 – List and concentration of nanoparticle solutions used in experiments.

NPs Size (nm)	Stock Solution Concentration (particles/mL)	100x diluted (particles/mL)	1 000x diluted (particles/mL)	10 000x diluted (particles/mL)	100 000x diluted (particles/mL)
500	$2{,}9 \times 10^{11}$	$2{,}9 \times 10^{9}$	$2{,}9 \times 10^{8}$	$2{,}9 \times 10^{7}$	$2{,}9 \times 10^{6}$
252	$5{,}7 \times 10^{12}$	$5{,}7 \times 10^{10}$	$5{,}7 \times 10^{9}$	$5{,}7 \times 10^{8}$	$5{,}7 \times 10^{7}$
230	$2{,}5 \times 10^{12}$	$2{,}5 \times 10^{10}$	$2{,}5 \times 10^{9}$	$2{,}5 \times 10^{8}$	$2{,}5 \times 10^{7}$

3.4.1 Nanoparticle concentration

For the commercial samples, concentrations provided by the manufacturer were used, while the 230 nm particles we characterized as follows. To start, we weighed an empty Eppendorf tube. Then, 300 mL of the 230 nm NP stock solution were pipetted into the same Eppendorf tube and left in a vacuum desiccator over-night. The weight of the Eppendorf was measured again. The Eppendorf was placed in the oven at 65 ºC for 4 hours to remove reaming liquid. The weight of the remaining powder was measured, and the solution concentration 1,7% w/v was calculated.

3.4.2 Dynamic Light Scattering

To further characterize the NPs, their zeta potential was obtained by Dynamic Light Scattering (SZ-100, HORIBA Scientific). The results are explained in section 7.4 of the Supporting Information.

3.5 Biological Experiments

In the biological experiments part of the project, we used human serum (H4522-20ML, Sigma-Aldrich) and a sample of purified extracellular vesicles (HCT116 EVs) provided by a collaborator.

4 Results and Discussion

4.1 Glass nanopipettes

In this section, we will be focusing on the study of the detection of NPs using glass nanopipettes. In Figure 4 it is represented a schematic of the obtained pipettes. A schematic for the glass nanopipette patch-clamp experiment set-up can be found in section 7.5 of the Supporting Information.

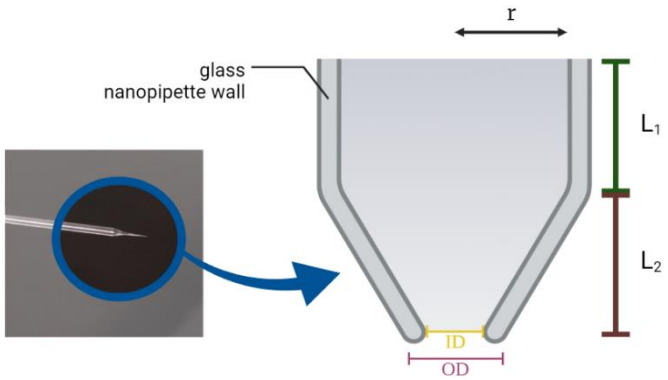

Figure 4 – Schematic of zoomed-in glass nanopipette.

One of the main features to study regarding nanopipettes is their resistance. The resistance of the pipettes can be divided into three components: the cylinder (Eq. 6), the cone (Eq. 7), and the sphere right at the entrance of the pipette (Eq. 8). The calculation of the resistance of the cone is more complex and fully explained in section 7.6 of the Supporting Information.

$$R_{\blacksquare} = \rho \frac{L}{A} = \frac{L_1}{\sigma \pi r^2} \tag{6}$$

$$R_{\Delta} = \frac{2L_2}{\sigma \pi r ID} \tag{7}$$

$$R_O = \frac{1}{\sigma 2 \pi ID} \tag{8}$$

The components dependent on the inner diameter (ID) of the pipette have a much higher resistance, as the ID is much smaller. Therefore, the cylinder component barely contributes to the overall resistance. Thus, the resistance is strongly dependent on the ID of the produced pipette.

4.1.1 Pipette Dimensions

After the nanopipettes were pulled from glass capillaries, the ones produced from Recipe 1 (Heat=549, Pull=0, Velocity=50, Time=250, Loop=3) were inspected using SEM (section 7.1.2 of the Supporting Information). The images were used to estimate the ID of the pipettes using the ImageJ software (Table 3).

Table 3 – Inner diameter of the nanopipettes produced from Recipe 1 and its corresponding resistance measured by Patch-Clamp.

	ID (nm)	Resistance (MΩ)
Pipette A	867 ± 21	7,6
Pipette B	671 ± 16	2,1
Pipette C	774 ± 58	1,6

As shown in Table 3, even though the recipe used to fabricate these pipettes was the same (Recipe 1), the dimensions vary, but what changes the most is the measured resistance, especially comparing Pipette A with the others. This shows that it is impossible to control the dimensions of the pipettes using the type of pipette puller available to us. Other authors that have used a laser pipette puller instead have shown promising results in using nanopipettes to detect nanoparticles using Resistive Pulse Sensing [33]–[35].

4.1.2 Particle Detection

The main goal of the glass nanopipettes study was the detection of NPs using patch-clamp and the resistive pulse-sensing method. Table 4 shows two examples of experiments done one after the other with different pipettes. The current graphs of these two experiments are shown in section 7.7 of the Supporting Information. In Example 2, there were over 1000 spikes registered (highlighted in green) but not a single spike in Example 1. Regarding the parameters used, the only difference was the pressure range. Even though a more extensive range was used in Example 1, that did not change the outcome, showing that the pressure range was not a factor.

Table 4 – Parameters used in two tests and the resistance measured by patch-clamp.

	Resistance (MΩ)	**Particles** (nm)	**Salt Concentration**	**Voltage** (mV)	**Pressure** (mbar)
Example 1	2,9	500	1 M PBS	35	50 to 300
Example 2	2,7	500	1 M PBS		50 to 150

However, there was a slight decrease in resistance, from one pipette to the other. These results show, how sensitive particle detection is. It is remarkable, how the slightest change in resistance, and therefore in the ID of the pipette, can affect the ability to detect NPs. It is possible to detect particles but not to reproduce results.

4.1.3 Summary

Overall, the main issue encountered with nanopipettes was the fabrication based on the available system used to produce these. As initially mentioned in the Materials and Methods section, this system used a filament as a heating source to melt the glass. The problem with this method is that the temperature of the filament will not be the same before experiments, as it depends on its cooling down after a pipette is pulled. As we pull new pipettes successively, the initial temperature of the filament would always be higher than before. This became an overwhelming issue, when pulling pipettes, because we were not able to reach stable resistance values between different measurements, and therefore unable to establish a clear relationship between measured resistance and pipette geometry.

As the initial step of the study of glass nanopipettes kept failing (the fabrication itself), the detection on NPs was almost impossible to achieve. Therefore, we focused the rest of the studies on a chip-based approach.

4.2 PDMS microfluidic chips

This section will focus on studying the use of PDMS microfluidic resistive pulse sensing chips to detect and quantify nanoparticles using pressure-driven flow. This is the central part and goal of this thesis. To achieve this, we used Patch-Clamp Amplifier to measure the small current changes as the particles move through the nanopore (Figure 5).

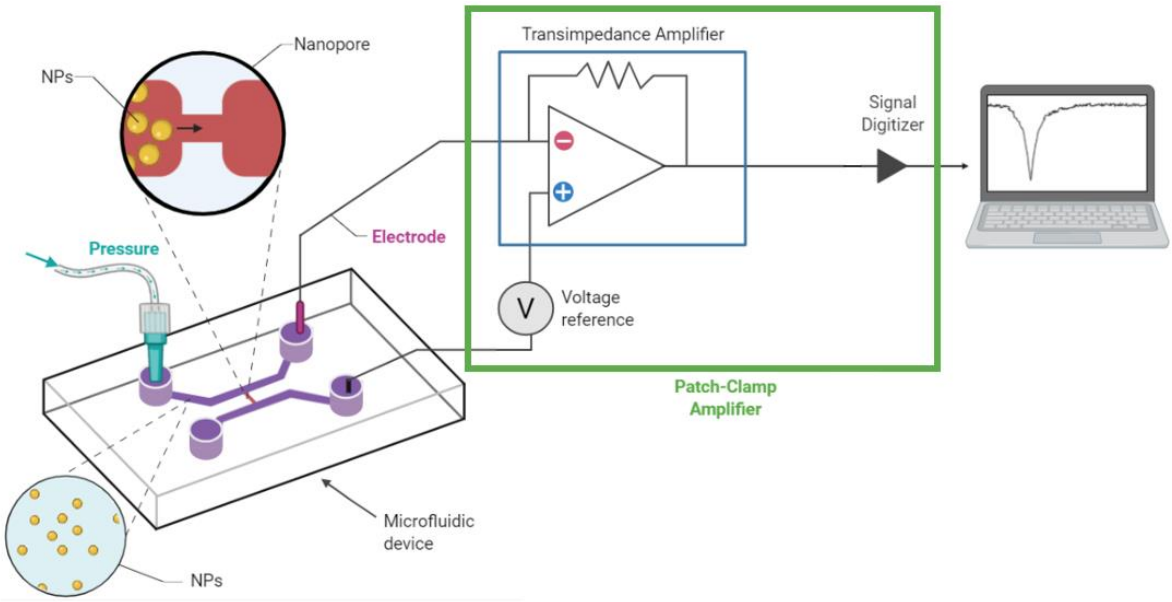

Figure 5 – Schematic of Patch-Clamp set-up and the fabricated PDMS microchips. Everything that was connected to the device during experiments is also represented: pressure controller (blue), electrode (pink), and reference electrode (black).

As explained in section 2.3 of the Introduction, this study will be performed using Resistive-Pulse Sensing. As a particle moves through the nanopore, this causes a drop in the current (spike). The spike width, amplitude, and frequency can give us information about the NPs in the solution and their concentration. The value of the two first parameters depend on the size of the particles passing through the pore and the geometry of the pore in the microfluidic device, and the frequency is related to the NP concentration.

The PDMS devices used in this project have channels with three structures: nano, micro, and macrochannels (Figure 6). Nanochannels can be divided into three types, according to their geometry. These can be smooth or have a single or double construction. The nanochannel connects the microchannels.

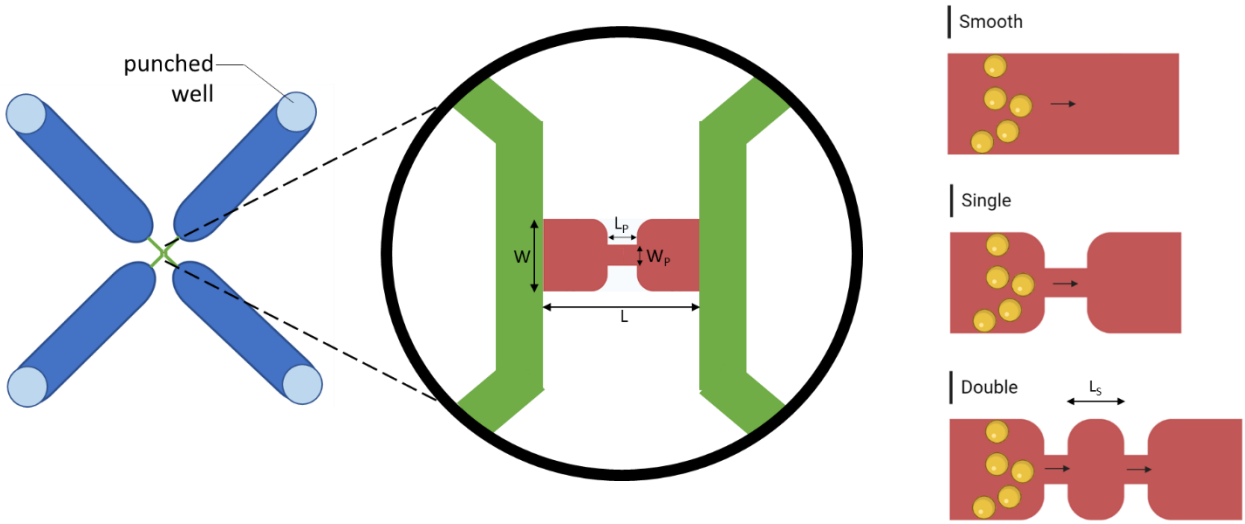

Figure 6 – Schematic of the PDMS chips with different structures: macrochannels (blue), microchannels (green), and nanochannel (red). There are three different types of nanochannel (smooth, single, and double constriction).

In Table 5 is represented the dimensions of the nanostructures for each chip design. According to the width of the nanochannel constriction, NPs were assigned to each design. A table with all the dimensions of the micro and macro structures is in section 7.9.1 of the Supporting Information (Table 21).

Table 5 – Chip designs and their dimensions. It is also represented, which NPs were used with each chip design.

Design	Channel type	Nanochannel dimensions			Constrictions dimensions			NPs used (nm)
		L (µm)	W (µm)	H (µm)	L_P (nm)	W_P (nm)	L_S (nm)	
2	Single constriction	15	15	1	500	600	-	230, 252 and 500
5	Smooth channel	15	1		-	-	-	252 and 500
7	Single constriction	15	7,5		500	600	-	230, 252 and 500
11	Double constriction	15	3		1000	500	500	230 and 252
12	Double constriction	15	3		1000	1000	500	500
13	Single constriction	15	3		1000	500	-	230 and 252

As mentioned previously, when a particle moves through the nanopore, it generates a current spike. Thus, as the spike parameters depend on the geometry of the pore, when we have a double constriction channel, this results in double spikes (Figure 7).

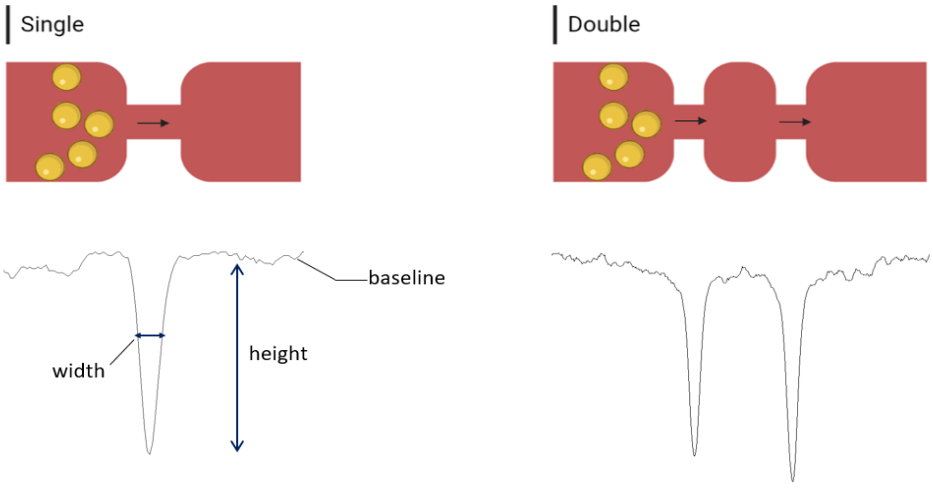

Figure 7 – Schematic of the relationship between pore geometry and the obtained current spikes. It is also highlighted, where the spike parameters (width and height) are taken.

Regarding the spike parameters, it is essential to understand what they mean. The current spike width indicates the time the particles take to cross the pore. The spike width is measured at half height. Another important parameter, that will be used a lot in later studies is the Relative Current spike Amplitude. This is taken from the current amplitude over the baseline value. Also, spike frequency should indicate concentration, which means a more concentrated solution should create more spikes than a lower concentrated solution. This will be studied and confirmed further in later sections.

In order to understand thoroughly, how the PDMS microfluidic chips work and their potential for the characterization of small particles, we will present and analyze it here through different studies. These include the influence of the nanochannel and the nanoparticle size in measurements, a pressure dependence study, a concentration study to determine the detection limit of the devices, and finally, the ability of the device to characterize biological samples, such as human serum and purified EVs. The results of the studies will be presented, discussed and conclusions will be made.

To understand how an In-house made RPS detection interface compares to a complex equipment (Patch-Clamp Amplifier), the same experiments will be performed on both types of equipment, then compared and discussed.

4.2.1 Theoretical calculations

The characterization of NPs using Resistive-Pulse Sensing is based on applying voltage and studying the current spikes. Therefore, it is important to study the expected resistance of the channels of each device beforehand, and the expected current amplitude shift that the NP should cause, when passing through the nanopore. Using these theoretical estimations, we can interpret our results and do further studies.

In Table 6 we show the resistance inside the structures of the device and the relative amplitude shift each particle can cause in low salt solutions. The total theoretical resistance results from the sum of the resistance caused by each channel structure. The equations used to obtain the values in Table 6 are in sections 7.9.1 and 7.9.2 of the Supporting Information.

Table 6 – Total theoretical resistance of the channels and the expected relative amplitude shift caused by the NPs in each design.

	R_{total} (MΩ)	I_{rel} (%)		
		230	252	500
Design 2	6,02	0,4215	0,5653	6,7688
Design 5	12,92	0,0681	0,0906	0,8837
Design 7	69,71	0,0364	0,0488	0,5848
Design 11	10,11	0,3686	0,4966	-
Design 12	7,99	-	-	1,4285
Design 13	7,88	0,4729	0,6371	-

For the interpretation of our results, we developed a mathematical relation between the relative current amplitude shift and the particle diameter (d) this shift corresponds to. This equation was obtained using Taylor series, and is given by:

$$d = \sqrt[3]{(W_P H_P)^2 R_{PP} \sigma - L_p W_p H_P} \qquad (9)$$

where R_{PP} is the resistance of the nanopore, when a particle is present. This parameter depends on the relative amplitude shift which influences the NP diameter. The equation for the R_{PP} can be found in section 7.9.3 of the Supporting Information alongside the steps to obtain Eq. 9.

In Table 7 we present the NP size corresponding to the expected relative amplitude shift calculated before and showed in Table 6. As these NP diameter values were obtained from a mathematical approximation (Eq. 9), it was important to calculate the relative error of this approximation as well. The errors were considered acceptable. These result from the approximations and assumptions made when developing Eq. 9.

Table 7 –Relative Amplitude shift and the corresponding NP diameter for each NP in different designs.

	Design	I_{rel} (%)	d (nm)	**Relative Error**
230	2	0,4215	237	3,12%
	5	0,0681	234	1,83%
	7	0,0364	237	3,12%
	11	0,3686	239	3,80%
	13	0,4729	237	3,80%

252	2	0,5653	262	3,80%
	5	0,0906	258	2,21%
	7	0,0488	262	3,80%
	11	0,4966	264	4,63%
	13	0,6371	264	4,63%
500	2	6,7688	598	19,68%
	5	0,8837	550	10,06%
	7	0,5848	598	19,68%
	12	1,4285	550	10,06%

As mentioned in section 2.2.1 of the Introduction, two critical aspects of the movements of NPs when they are suspended in an electrolyte are electrophoresis and the electroosmotic flow, as they are responsible for the electrical transport.

In Table 8 we have the expected electroosmotic and electrophoretic velocity values in low salt solutions. These were calculated from the respective mobility values and the field strength using Eq. 3. The equations and values used to calculate the field strength are in section 7.9.4 of the Supporting Information. In the case of the electrophoretic mobility, the value was obtained using DLS during Zeta Potential measurements on low salt solutions. The electroosmotic mobility and velocity were alsocalculated for high salt solutions (section 7.9.4 of the Supporting Information).

These results confirm that electroosmosis and electrophoresis act in opposite directions, but in similar magnitudes, as EOF is a little larger than EP.

Table 8 – Field strength in the pore, mobility, and velocity (electroosmotic and electrophoretic) for each design on low salt solutions.

	$\boldsymbol{E}$ (V/m) (V=100mV)	$\boldsymbol{\mu_{EOF}}$ ($m^2/V{\cdot}s$) [36]	$\boldsymbol{v_{EOF}}$ (m/s)	$\boldsymbol{\mu_{EF}}$ ($m^2/V{\cdot}s$)	$\boldsymbol{v_{EF}}$ (m/s)
Design 2	$2{,}00 \times 10^{5}$	$1{,}50 \times 10^{-8} \pm 0{,}30 \times 10^{-8}$	$3{,}00 \times 10^{-3}$	$-1{,}19 \times 10^{-8} \pm 2{,}68 \times 10^{-9}$	$-2{,}38 \times 10^{-3}$
Design 5	$6{,}67 \times 10^{3}$		$1{,}00 \times 10^{-4}$		$-7{,}94 \times 10^{-5}$
Design 7	$2{,}00 \times 10^{5}$		$3{,}00 \times 10^{-3}$		$-2{,}38 \times 10^{-3}$
Design 11	$5{,}00 \times 10^{4}$		$7{,}50 \times 10^{-4}$		$-5{,}95 \times 10^{-4}$
Design 12	$5{,}00 \times 10^{4}$		$7{,}50 \times 10^{-4}$		$-5{,}95 \times 10^{-4}$
Design 13	$1{,}00 \times 10^{5}$		$1{,}50 \times 10^{-3}$		$-1{,}19 \times 10^{-3}$

Besides analyzing the electrical transport, responsible for the electroosmosis and electrophoretic effects in the nanopore, it is important to characterize the pressure-driven flow, namely the flow rate, and the hydraulic resistance and velocity. In Table 9 we have the relationship between the hydrodynamic resistance in the nanochannel and the flow rate. This was calculated following Eq. 4. The hydrodynamic resistance was obtained according to the geometry of the nanopore. The equations used are in section 7.9.5 of the Supporting Information. These results show how the flow rate increases with pressure.

Table 9 – The hydrodynamic resistance of the nanochannel and the corresponding flow rate for each design.

	$\boldsymbol{R_{hydNANO}}$ ($Pa{\cdot}s/m^3$)	$\boldsymbol{Q}$ (m^3/s)			
		50 mbar	100 mbar	150 mbar	200 mbar
Design 2	$9{,}82 \times 10^{16}$	$2{,}55 \times 10^{-14}$	$5{,}09 \times 10^{-14}$	$7{,}64 \times 10^{-14}$	$1{,}02 \times 10^{-13}$
Design 5	$3{,}79 \times 10^{17}$	$6{,}59 \times 10^{-15}$	$1{,}32 \times 10^{-14}$	$1{,}98 \times 10^{-14}$	$2{,}64 \times 10^{-14}$

Design 7	1,18 x 10^{18}	2,11 x 10^{-15}	4,23 x 10^{-15}	6,34 x 10^{-15}	8,45 x 10^{-15}
Design 11	3,62 x 10^{17}	6,91 x 10^{-15}	1,38 x 10^{-14}	2,07 x 10^{-14}	2,77 x 10^{-14}
Design 12	1,22 x 10^{17}	2,04 x 10^{-14}	4,09 x 10^{-14}	6,13 x 10^{-14}	8,17 x 10^{-14}
Design 13	2,15 x 10^{17}	1,16 x 10^{-14}	2,33 x 10^{-14}	3,49 x 10^{-14}	4,66 x 10^{-14}

Table 10 shows the hydrodynamic velocity in the nanopore. This relation is established by Eq. 5. As expected, the hydrodynamic velocity increases with the pressure applied.

Table 10 – Hydrodynamic velocity for each design depending on pressure applied.

	Cross sectional area (m^2)	v_{hyd} (m/s)			
		50 mbar	100 mbar	150 mbar	200 mbar
Design 2	6,00 x 10^{-13}	0,042	0,085	0,127	0,170
Design 5	1,00 x 10^{-12}	0,007	0,013	0,020	0,026
Design 7	6,00 x 10^{-13}	0,004	0,007	0,011	0,014
Design 11	5,00 x 10^{-13}	0,014	0,028	0,041	0,055
Design 12	1,00 x 10^{-12}	0,020	0,041	0,061	0,082
Design 13	5,00 x 10^{-13}	0,023	0,047	0,070	0,093

These theoretical calculations allowed us to compare the velocity of the flow caused by electrical transport phenomena and the velocity caused by pressure-driven flow. We observed that no matter the pressure applied, the hydrodynamic velocity is at least 130 times bigger than both electroosmotic and electrophoretic velocity. In other words, the order of magnitude of the electroosmotic and electrophoretic velocity values is 3 to 4 times smaller than the order of magnitude of the hydrodynamic velocity. This proves that pressure-driven flow dominates the transport in the electrolyte solution. This also happens because we applied low voltages, ranging from 30 to 100 mV, and as electrical transport strongly depends on the voltage applied, it has less effect.

4.2.2 Pressure Dependence

As shown by the previous section, pressure-driven transport dominates over electrical transport when low voltages are applied to the system. To study this further we analyzed how the height and width of the spikes changed with increasing pressure (Figure 8). Figure 8B shows that pressure driven-flow does not affect the amplitude of the current spikes significantly, while Figure 8C shows that their width decreases with increasing pressure, as the particles become faster, as expected by the calculations done before (Table 10) and confirmed by the results of Figure 8D. This figure shows that pressure and velocity, in ideal measurements, are directly proportional. The velocity results from an approximation of 1 over the spike width. However, we soon noticed that getting these ideal measurements can be difficult. This is the case due to clogging or other identified common behaviors. This pressure dependence study allowed us to identify many common behaviors among devices no matter the design and particles used. This will be discussed in the next section.

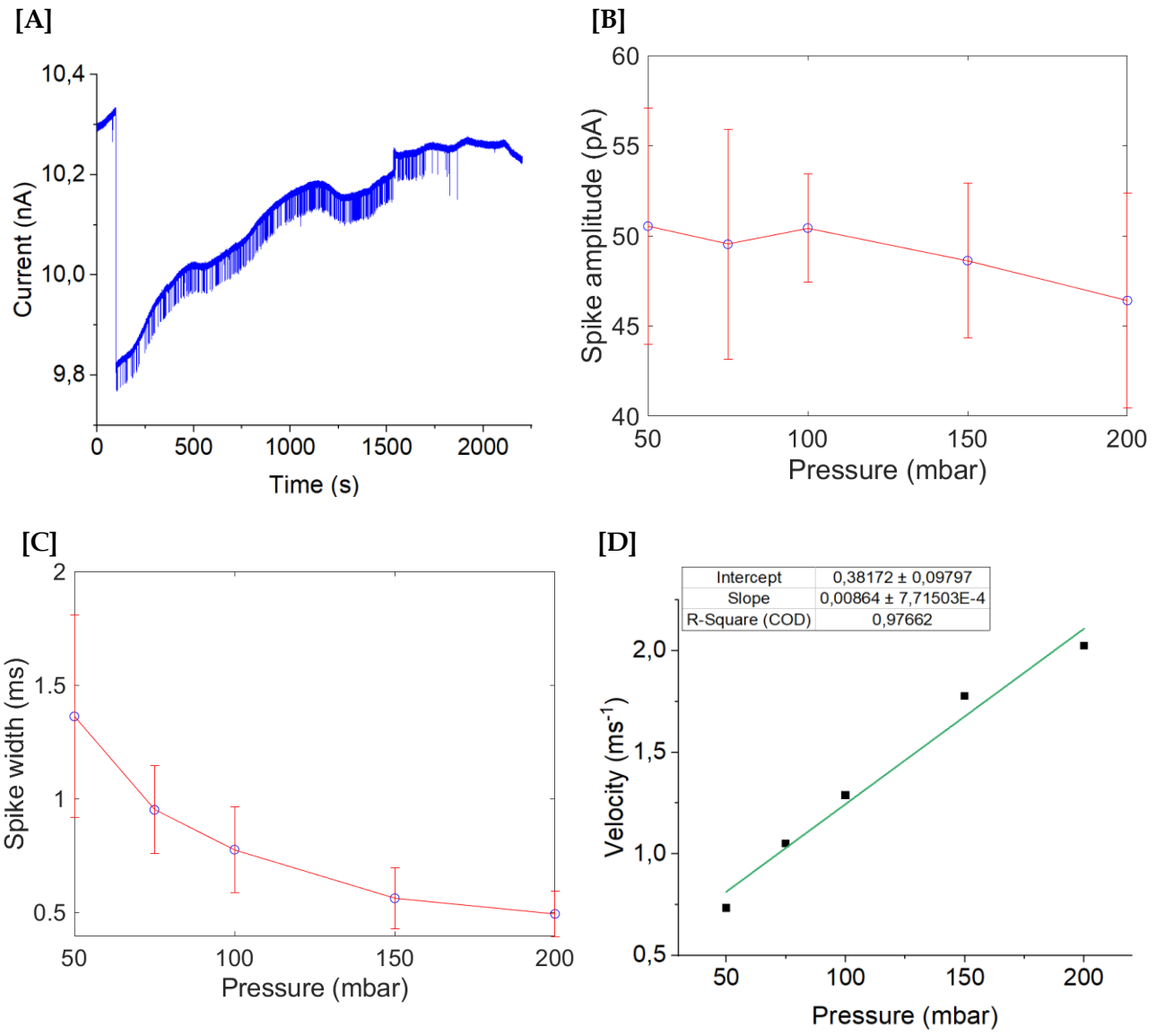

Figure 8 – Ideal device data and behavior: [A] Raw data, [B] Spike amplitude vs. pressure applied, [C] Spike width vs. pressure applied, and [D] particle velocity in function of the pressure applied. Data set obtained with Design 5 and 500 nm NPs.

4.2.3 Device behaviors and measurements scenarios

Many experiments were done with the PDMS chips, and even though different designs and particles were used, it is possible to identify common behaviors and categorize them. We divided these behaviors into three scenarios: ideal, working, and non-working. The behaviors identified were categorized based on the presence of spikes, how the parameters of the spikes are affected by the increase of pressure, the number of data points in the width and amplitude vs. pressure graphs, and clogging.

One aspect that prevents the detection of nanoparticles is the clogging of the pore. To be able to identify clogging is a crucial step in data analysis. Clogging is associated with the decrease of the measured current as the resistance in the pore increases, due to the decrease of area available in the pore, because of its partial blocking by other NPs. Clogging can also be anticipated when spikes become broader, meaning they take more time to cross the pore

Before analyzing the results obtained, we defined a frequency “rule” to help categorize them. This rule states that for a file to be worth analyzing, it needs to have at least 100 spikes in 100 s.

All the graphs representing the categorized behaviors, such as the pressure dependence of the width and amplitude of the spikes, and raw data, are in section 7.8 of the Supporting Information. The behaviors of the

devices were categorized as follows:

A. Ideal device: Many spikes registered, so it obeyed the frequency "rule". The amplitude of the spikes was almost unchanged, but the width of the spikes decreased as we increased the pressure. The increasing pressure did not affect the current amplitude but made the NPs take less time passing through the nanopore (Figure 8).
B. Working device
    - Only one data point in the width and amplitude vs. pressure graphs but obeyed the frequency rule. This was caused by the clogging of the chip when other values of pressures were applied. It was not possible to identify a specific pressure that made this happen more often (Supplementary Figure 20A).
    - It was possible to identify three variations of the behavior of the chip after it clogs: it either clogs and does not unclog again, only unclogs at the end of the experiment, or it unclogs straight away.
        - There was a sudden clogging, the current dropped, and it did not have spikes until the end of the experiment, or if it did, they were very few. This clogging was usually anticipated by the increase of the width of the spikes as the pressure applied increased. Spike current amplitude either stayed within the same value or decreased before it clogged (Supplementary Figure 20B).
        - After the clogging and by increasing the pressure, it unclogged later on, and we registered spikes again. In this case, the amplitude of the spikes stayed almost unchanged, as pressure increased, and width decreased. Right before it clogged, the width increased a little. When there were spikes again, they had less current amplitude, this indicates that before there was something partially blocking the pore, which led to clogging that is not present anymore. The width was also smaller than before, but it was due to the higher pressure applied (Supplementary Figure 20C).
        - When the device clogged but unclogged straight away. In this case the amplitude of the spikes decreased with the pressure, but during the clogging (there were fewer spikes) the amplitude increased and then stabilized, as it unclogged. The width of the spikes decreased with pressure (Supplementary Figure 20D).
    - There were only a few spikes registered, and these were spaced out. However, it obeyed the frequency "rule" (Supplementary Figure 20E). Spikes were spaced out because the device was getting clogged, as the width of the spikes increased.
    - Experiments where the baseline is unstable. In these cases, the chip worked as we registered many spikes, but the constant shifts of the baseline made the analysis difficult. When this happened, the software used to process the files would wrongfully mark noise as spikes in some of the sections of the experiments. Therefore, a complete analysis of these results was not made (Supplementary Figure 20F).
C. Non-working devices
    - Results where it did not have any spikes, or if it had spikes, they were only a few and did not obey the frequency "rule" (Supplementary Figure 21A).
    - It registered a few spikes at the start, clogged and then had many bubbles going through the pore until the end of the experiment (Supplementary Figure 21B).
    - Experiments where the noise was higher than usual, it was difficult even to see if there were small spikes masked by such huge noise (Supplementary Figure 21C).

4.2.4 Design Optimization

Before doing a study with a device we needed to determine which chip and particle solution combination worked better, thus this study was the first to be completed. This is crucial as it dictates, which designs, and NPs were used in the more specific studies later. For a chip design to be considered good it had to pass two tests: i) both HC and LC combinations for a particular particle and design had to have a success rate above 30%. The NP and device combination, that passed that test, ii) went through an analysis of the measured relative spike current amplitude to check, if it agreed with the theoretical expectation. Even though a device detected spikes, the data still needed to be thoroughly analyzed, before the chip design was considered good.

In Table 11 we have the obtained success rates for spike detection of all possible combinations and the quantity of experiments done for each combination. An experiment was considered a success, when spikes were registered, and it obeyed the frequency "rule" mentioned before. The combination of 252 nm NPs on a high salt solution with Design 5, was not tested as we noticed that no matter the design, 252 nm NPs were not working with high salt solutions.

Table 11 – The success rate for spike detection obtained for each NP, device design and solution combination.

			Design 2	**Design 5**	**Design 7**	**Design 11**	**Design 12**	**Design 13**
1 M PBS (High salt)	100x diluted (HC)	230	28,57% (N=7)	-	28,57% (N=7)	71,43% (N=7)	-	28,57% (N=7)
		252	0,00% (N=7)	-	0,00% (N=7)	0,00% (N=7)	-	0,00% (N=7)
		500	28,57% (N=7)	62,50% (N=8)	57,14% (N=7)	-	66,67% (N=9)	-
	1 000x diluted (LC)	230	0,00% (N=7)	-	0,00% (N=7)	14,29% (N=7)	-	14,29% (N=7)
		252	0,00% (N=7)	-	0,00% (N=7)	0,00% (N=10)	-	0,00% (N=7)
		500	57,14% (N=7)	28,57% (N=7)	28,57% (N=7)	-	42,86% (N=7)	-
137 mM PBS (Low salt)	100x diluted (HC)	230	85,71% (N=7)	-	42,86% (N=7)	28,57% (N=7)	-	85,71% (N=7)
		252	42,86% (N=7)	57,14% (N=7)	14,29% (N=7)	50,00% (N=8)	-	37,50% (N=8)
		500	28,57% (N=7)	60,00% (N=10)	50,00% (N=8)	-	57,14% (N=7)	-
	1 000x diluted (LC)	230	58,33% (N=12)	-	57,14% (N=7)	14,29% (N=7)	-	12,50% (N=8)
		252	57,14% (N=7)	75,00% (N=8)	66,67% (N=9)	20,00% (N=10)	-	14,29% (N=7)
		500	0,00% (N=8)	33,33% (N=9)	57,14% (N=7)	-	50,00% (N=8)	-

As the first test required the device design and NP combinations to have at least a 30% success rate for both particle concentrations, we discarded the combinations with high salt for further analysis. Of the 24 combinations done with high salt only 6 had a success rate above 30%, and only one device and NP combination (Design 12 with 500 nm NPs) had a success rate above 30% for both high and low concentration solutions.

Therefore, no further experiments were done with high salt PBS solutions.

Based on tests with low salt PBS solutions, Design 11 and Design 13, were discarded for all NP sizes used. Also, Design 2 with 500 nm NPs and Design 7 with 252 nm NPs were discarded. Therefore, we proceeded with 14 combinations for the second test.

The second test is focused on the relative amplitude and NP diameter analysis. This is the final and most important step in categorizing the devices as it allows to determine, which results are in agreement with the theoretical calculations. In this test the HC and LC are analyzed together as particle concentration does not influence the measured current (Table 12). This table shows the average measured relative amplitude and the average expected NP size. It is also represented the standard deviation corresponding to these.

Table 12 – Relative Spike Amplitude and Expected NP diameter analysis for the combinations that passed the first test. The measured relative amplitude shift was taken at 100 mbar.

	Design 2		**Design 5**		**Design 7**		**Design 12**
	230	**252**	**252**	**500**	**230**	**500**	**500**
Expected Relative Amplitude (%)	0,4215	0,5663	0,0906	0,8837	0,0364	0,5848	1,4285
Measured Relative Amplitude (%)	0,3513 ± 0,2067 (N=13)	0,3079 ± 0,1412 (N=7)	0,0720 ± 0,0250 (N=10)	0,4693 ± 0,0361 (N=9)	0,3599 ± 0,1851 (N=7)	0,3395 ± 0,2940 (N=8)	0,3606 ± 0,1968 (N=8)
Expected NP size (nm)	215 ± 42 (N=13)	210 ± 29 (N=7)	233 ± 28 (N=10)	447 ± 12 (N=9)	492 ± 93 (N=7)	470 ± 115 (N=8)	339 ± 53 (N=8)
Accuracy	15,95%	18,79%	10,12%	10,93%	113,94%	18,41%	32,12%
Precision	19,61%	13,69%	11,95%	2,59%	18,96%	24,41%	15,70%

The data in Table 12 shows the precision (dispersion of individual values) and accuracy (deviation of average from expected value) of our successful measurements. By analyzing the results, we discarded the combination of Design 7 with 230 nm NPs, due to the low accuracy, which meant that the measured values were far from the actual diameter of the NPs.

Based on tests with Design 5, we observed that both NPs have similar accuracy errors, meaning the measured relative amplitude values are about 10% smaller than the expected values. This is a calibration issue, but the device still performs very well. The combination of Design 5 with 500 nm NPs gives precise results, as the difference between measurements is small.

Regarding the experiments done on Design 2, we can see that the device cannot correctly resolve the differences in size, as the measured relative amplitude are very similar for both NPs. Another aspect is that no matter the particle size, the measurements do not have enough accuracy.

Other designs and NPs combinations were not discarded, but the accuracy and precision capability of each device was considered, when deciding which devices to use for each study. For the concentration study we used Design 5 with 500 nm NPs, Design 2 with 230 nm NPs, and Design 12 with 500 nm NPs. In this study the accuracy and the precision of the device are not critical as the detection ability was the main focus. It was also important to have an example of each channel type to understand if that would influence the detection limit. In the mixing study we used the device that could detect two different NP sizes with high accuracy and precision, Design 5. For the biological experiments we used Design 2 and Design 5, as the goal of that study

was to identify different sizes of populations, thus there was need to choose devices able to cover a broad range of sizes, while still maintaining high accuracy and precision.

4.2.5 Pulse Shape Analysis

Further pulse analysis was done to complement the device optimization study. In this section we studied the average width of the spikes per design, the velocity of the particles, when passing through the pore and how that compares with the theoretical calculations, and finally, an analysis of the shape of the double spikes.

To study how the width of the spikes differs among designs, we compared the average spike width at 100 mbar (Table 13). The results show that the average spike width is dominated by the pressure applied, and thus, the hydrodynamic velocity, as the spike width is very similar for all designs, except for double constriction. Nevertheless, the velocity for double and single constriction channels is also similar. In terms of velocity values, Design 5 has a much higher measured hydrodynamic velocity, than the other designs, caused by the wider smooth channel (W=1000nm). However, there is a discrepancy between the measured hydrodynamic velocity and the estimated one (Table 10). It is likely that the approximations and assumptions made to calculate the values in Table 10, led to the difference between the measured and estimated values.

Table 13 – Average spike width at 100 mbar. Comparison between the velocity from experimental data and the hydrodynamic velocity obtained in section 4.2.1.

	NP Diameter (nm)	Average spike width (ms)	Pore length (nm)	Measured velocity (m/s)	v_{hyd} (m/s) (from Table 10)
Design 2	230	0,4227 ± 0,1291	500	0,0011	0,0850
	252	0,4159 ± 0,0666		0,0012	
Design 5	252	0,4302 ± 0,1967	15000	0,0349	0,0130
	500	0,4183 ± 0,0778		0,0359	
Design 7	500	0,3818 ± 0,1213	500	0,0013	0,0070
Design 12	500	0,6173 ± 0,2087	1000	0,0016	0,0410

In this project we had three pore types available to use, and as explained before, the geometry of the pores strongly influences the current spikes, especially in the case of double constriction channels. Figure 9A is an example of the double spikes registered with Design 12 and 500 nm NPs. When passing the pores, the double spikes should have the same amplitude. However, in the third pair of spikes we can see that the first spike had higher amplitude than the second spike, this meant the first pore might have been temporally blocked by other NPs or, as the difference in amplitude is not that significant, it results from the size deviation of the NPs. This effect can be more predominant at times and indicate the clogging of one of the pores. This figure also shows that the particles move extremely fast, producing "sharp" spikes. In this example, it took 0,65 ms for the NPs to cross each pore and 0,95 ms going from one pore to the other, which agrees with the fact that the pore separation is longer than the pore itself.

Another important aspect of the analysis of double spikes is latency (Figure 9B), the time it takes for particles to cross the pore. In the case of single constriction channels, the movement of the particles through the pore follows a Poisson process, proving that the particles move through the pore independently, without affecting each other [37]. On the other hand, double constriction channels partially follow a Poisson process, because the first spike is caused by independent movement, but the second spike depends on the first. The movement of the NP through the second pore caused a bump in the exponential decay describing the latency in Poisson distribution, which represents the time to cross from pore-to-pore.

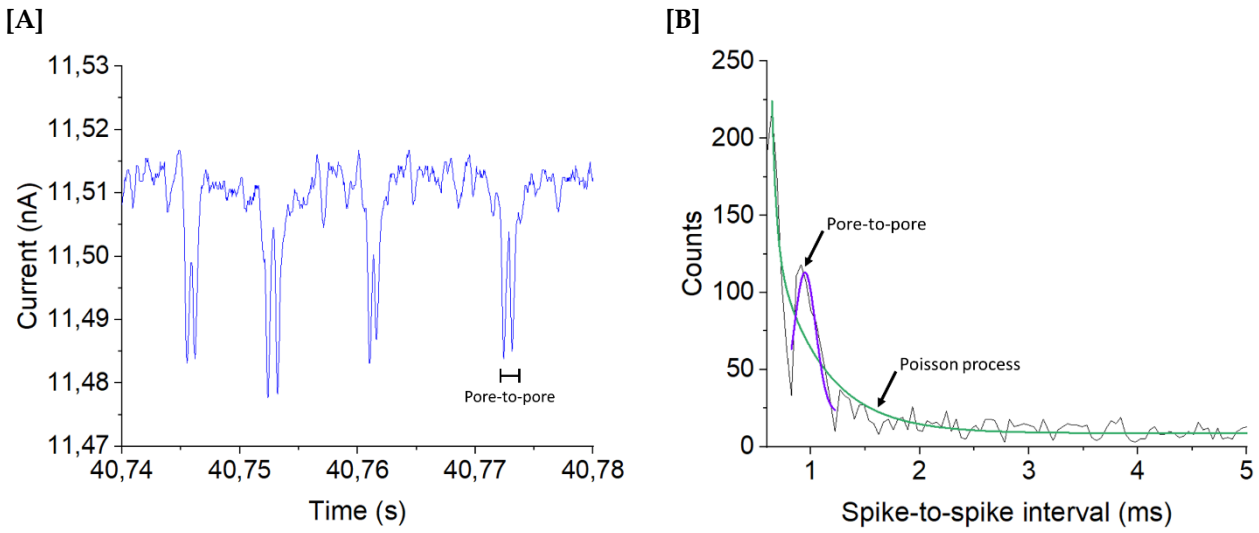

Figure 9 – [A] Raw signal of double spikes measurements in Design 12 with 500 nm NPs, and applying 75 mbar, and corresponding [B] latency histogram. In the latency histogram is represented the exponential decay of Poisson process (green) and a Gaussian distribution (purple).

4.2.6 Concentration study

To further analyze the potential of these microfluidic chips, a concentration study was performed. In order to do that, the solution concentration was progressively increased between measurements in the same chip but maintaining the same salt concentration and NPs used. This is a critical study, as it allows us to establish the concentration detection limit of the devices. Table 2 in section 3.4 of Materials and Methods shows the concentration of NPs corresponding to each diluted solution.

The concentration study was performed in the three different channel types (smooth, single, and double constriction channels). To focus on the effects of concentration change, the voltage and pressure applied were the same within the same chip. In the case of the smooth channel, the experiments were done on Design 5 with both high and low salt concentrations and using 500 nm NPs. For the single constriction channel, Design 2 was used with 230 nm NPs on a low salt concentration solution. Lastly, for double constriction channels, experiments were performed using Design 12 with 500 nm NPs on a high salt concentration solution. These were the combinations selected as they had the highest success rate in their channel type.

To establish a relationship between the number of spikes over time and the concentration of the solution, we plotted the frequency in function of that concentration (Figure 10).

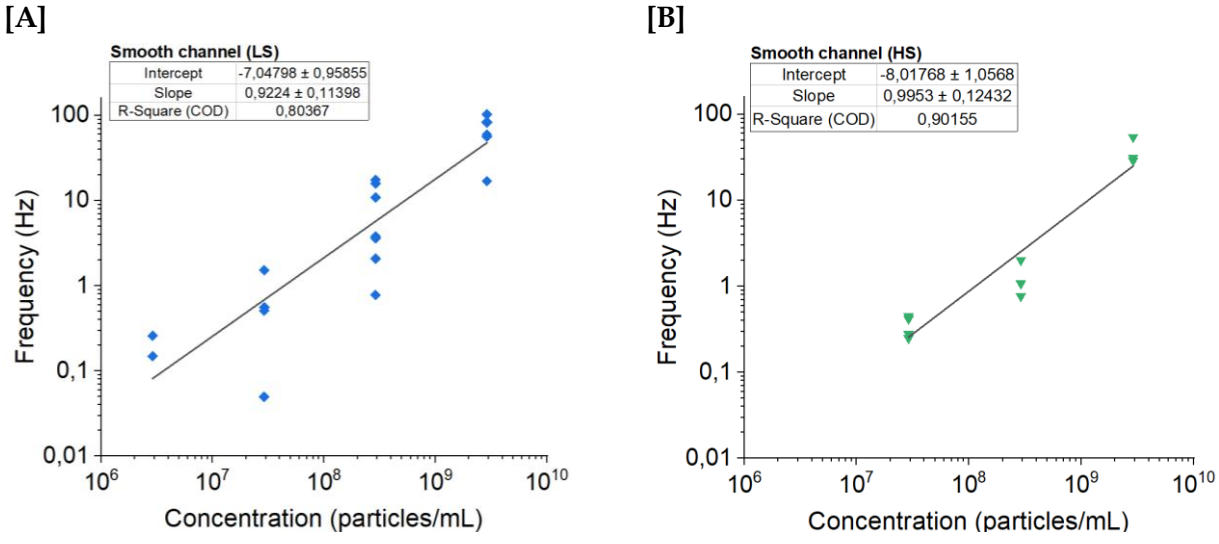

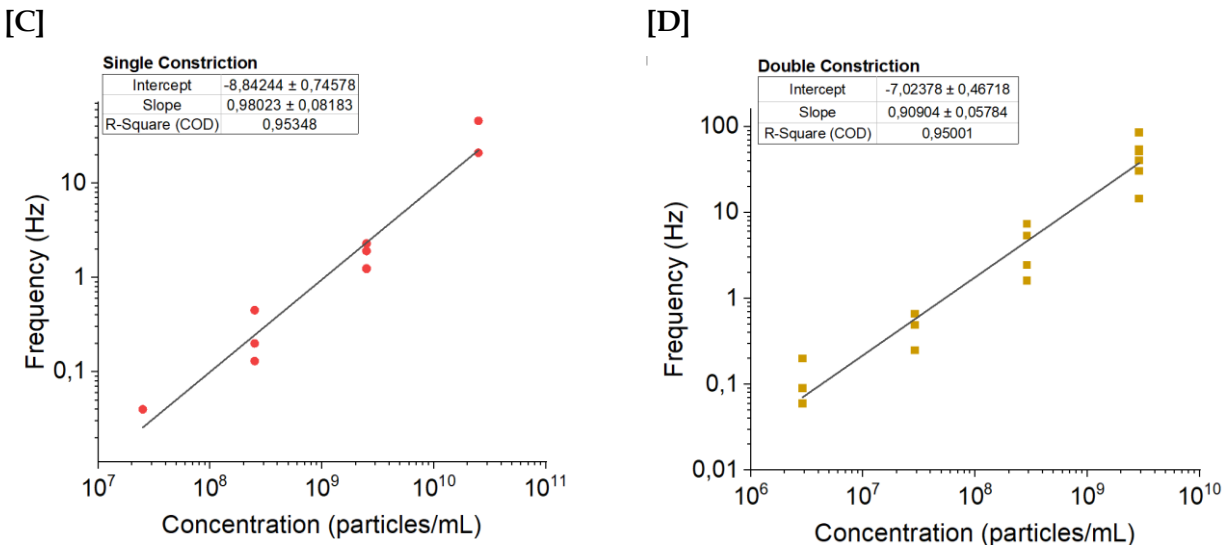

Figure 10 – Graphs of spike frequency vs. the particle concentration, using log-log regressions. For [A], [B] smooth, [C] single, and [D] double constriction channels. The spikes were counted in the 100 or 150 mbar region of the measurements.

The slope and the intercept values of the log-log linear regressions are represented in Table 14. A relationship between these values can be established using Eq. 10, where f is the spike frequency (Hz), and C is the concentration (particles/mL).

$$\log f = \log b + m \log C \Leftrightarrow \log f = \log b + \log C^m \Leftrightarrow \log f = \log bC^m \Leftrightarrow$$

$$\Leftrightarrow f = bC^m \ (Hz) \qquad (10)$$

Table 14 – Slope and intercept value of the linear regression for each channel type.

	m	log(b)	b [Hz/(particles/mL)]
Smooth Channel (LS)	0,92240	-7,04798	8,95406 x 10^{-8}
Smooth Channel (HS)	0,99530	-8,01768	9,60108 x 10^{-9}
Double Constriction	0,90904	-7,02378	9,46717 x 10^{-8}
Single Constriction	0,98023	-8,84244	1,43734 x 10^{-9}

Analyzing the graphs obtained and the slope values, we see that they are all positive and close to 1. This means that the frequency is linearly proportional to concentration. Therefore, as the solution has more particles, the spike frequency increases, as expected. Thus, Eq. 11 can be changed to:

$$f = bC \ (Hz) \qquad (11)$$

Focusing now on Eq. 11, the parameter b is the constant of proportionality. When b is higher this means that the device is more sensitive, as it can detect spikes for lower concentrations. The highest b value registered was approximately 10 x 10^{-8} =10^{-7} [Hz/(particles/mL)] for a double constriction channel. Moreover, since the start, we established a minimum of 100 spikes per 100 s for an experiment to be considered good and worth analyzing. Therefore, a good experiment needs to have at least a spike frequency of 1 Hz. Thus, considering the highest b value registered and the frequency "rule", the detection limit of the device is 10^7 particles/mL. Below this concentration, it is unlikely to register any spikes. Another way of demonstrating this detection limit is by calculating the expected spike frequency using Eq. 10 with the slope and intercept values for each channel type (Table 15).

Table 15 – Expected spike frequency (Hz) depending on solution concentration for each channel type.

	NPs (nm)	**2,9 x 10^9 (particles/mL)**	**2,9 x 10^8 (particles/mL)**	**2,9 x 10^7 (particles/mL)**	**2,9 x 10^6 (particles/mL)**
Smooth Channel (LS)	**500**	47,88	5,72	0,68	0,08
Smooth Channel (HS)		25,13	2,54	0,26	0,03
Double Constriction		37,84	4,67	0,58	0,07
		2,5 x 10^{10} (particles/mL)	**2,5 x 10^9 (particles/mL)**	**2,5 x 10^8 (particles/mL)**	**2,5 x 10^7 (particles/mL)**
Single Constriction	**230**	22,38	3,34	0,25	0,02

The expected frequency values in Table 15 demonstrate that as the solution decreases its concentration, there is a considerable drop in spike frequency until it approaches a minimum value of 0 Hz. No matter the stock solution concentration, the expected spikes frequency of 500 and 230 nm NPs approaches 0 after three dilutions. This means that for a particle concentration between the range of 10^7 and 10^8 particles/mL we are within the detection limit, confirming the estimation made before.

For the case of the Smooth channel type, both high and low salt concentration solutions were tested to see how this concentration would affect the spike detection. The difference between them is that the device has a lower detection limit for high salt concentration solutions. It does not detect any spikes for a concentration of 2,9 x 10^6 particles/mL. Two factors contribute to this: pressure-driven flow works better in lower salt solutions, explained in section 2.2.2 of the Introduction, and as determined above, that concentration is below our detection limit.

Overall, this study now allows us to calculate the expected spike frequency from the desired solution concentration, and most importantly, estimate the detection limit of the devices. To properly quantify particles and gather enough data to characterize them, it is not recommended to do dilutions below a concentration of 10^8 particles/mL. Lower than that, spikes are detected but not in enough quantity to gather pertinent information about the NPs in question. Considering the frequency "rule", if the expected spike frequency for a particular concentration is below 1 Hz, the results will not be quantifiable. Besides that, this study confirms that there is a direct relationship between frequency and concentration

4.2.7 NP mixture study

One of the main goals of this project is to distinguish different particle sizes in the same sample. In order to test this, we chose Design 5 due to the larger channel width, and because this was the device with higher accuracy and precision, as established in the Design Optimization analysis (section 4.2.4). Before starting this study, we analyzed the Expected Relative Current shift and the Expected NP diameter NP (Table 16). The Expected NP diameter was calculated using the equation developed in this project (Eq. 9 explained in section 7.9.3 of the Supporting Information). This equation establishes a relationship between the theoretical expected relative amplitude and the NP diameter that it represents.

Table 16 – Expected relative current amplitude shift and NP diameter for each particle in Design 5. The associated relative error of the approximation was also calculated.

NP diameter (nm)	Expected Relative Amplitude (%)	Expected NP Diameter (nm)	Relative Error
230	0,0681	234	1,83%
252	0,0906	258	2,21%
500	0,8837	550	10,06%

As shown in Table 16, the relative amplitude expected for the 230 and 252 nm NPs is very small and similar. Besides that, the 230 nm NPs were research samples, unlike the commercial 252 and 500 nm ones. Therefore, it is expected that 230 nm NPs have less size uniformity, which may overlap with the 252 nm NPs. Thus, to fully evaluate the distinctive abilities of the device, 252 and 500 nm NPs were mixed in ~2:1 ratio, $5{,}7x10^9$ and $2{,}9x10^9$ particles/mL, respectively, while the 230 nm NPs were not considered in this study.

To identify the different NP populations, we focused on the Expected NP diameter, calculated from the Relative Amplitude Shift that the NP causes when passing through the pore (Figure 11).

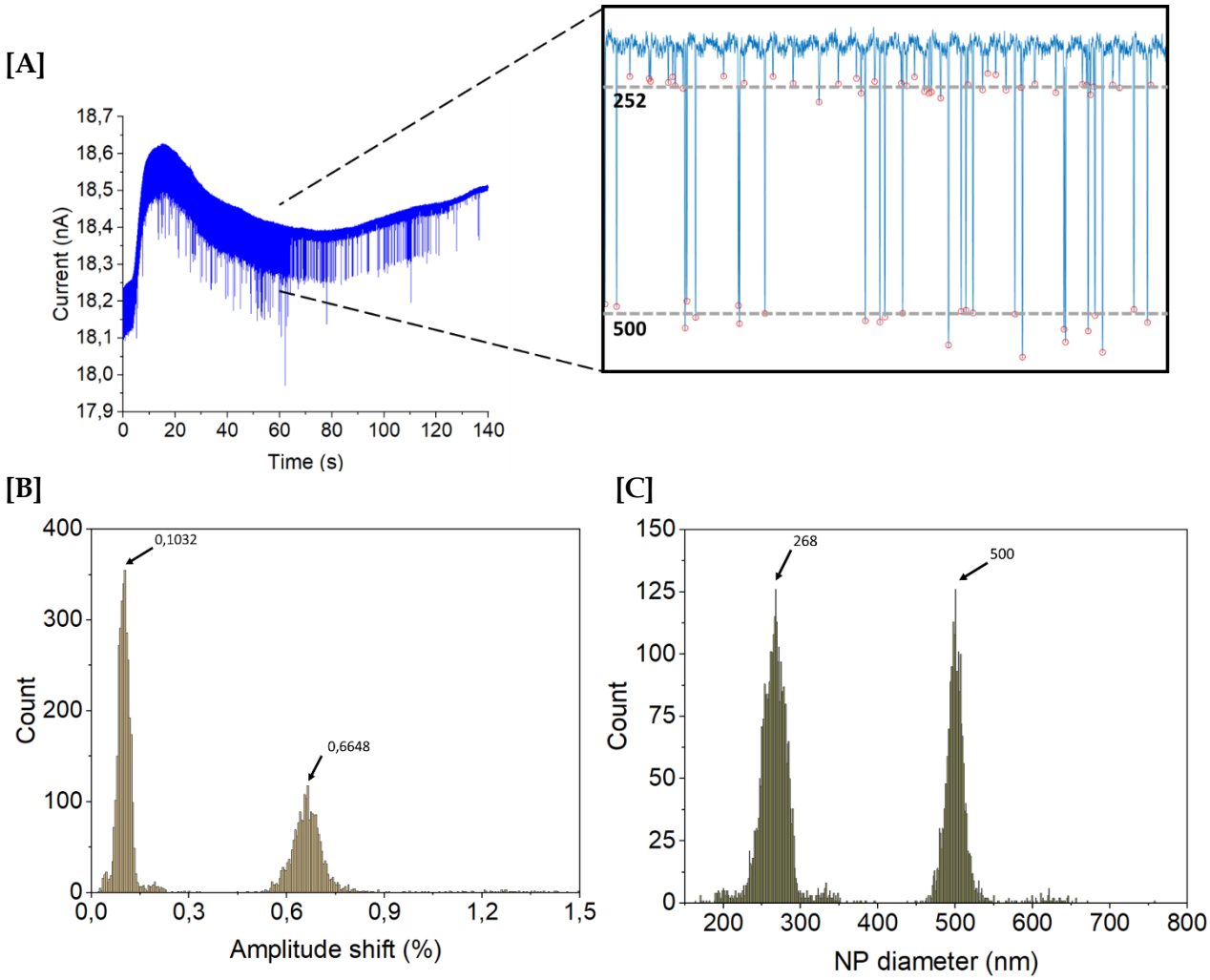

Figure 11 – [A] Raw data with the registered spikes marked in red and the two populations identified with a dashed line (not accurate, just representative). [B] Histogram of the Expected Amplitude shift. [C] Histogram of the Expected NP diameter of the NPs mixed together. The identified populations are marked by black arrows. Only 100 and 150 mbar were applied during this measurement.

Figure 11C shows two distinct populations centered at 268 and 500 nm that correspond to the 252 nm and 500 nm NPs, respectively. The population corresponding to the 500 nm NPs is very accurate as the expected size matches the actual size. That population is also relatively narrow meaning there is not much deviation,

which was confirmed by the width at half maximum, 19,5 nm, that corresponded to a 10 nm standard deviation. This deviation is close to the one provided by the manufacturer of these NPs, 6 nm.

However, for the population corresponding to the 252 nm NPs, there was a shift to the right, which is in agreement with the current amplitude population center. There is not a significant difference in the Expected Relative Amplitude value and the measured one, 0,0906% and 0,1032% (Table 16 and Figure 11B). However, that translates into a more considerable difference between the expected NP diameter and the real one. This shows how sensitive to size the system is. Moreover, in the case of this population, the width at half maximum was 35,7, which translated into a higher standard deviation of 18 nm, instead of the expected 6 nm. This higher standard deviation could indicate that this device has more difficulty in accurately identifying smaller NPs. Nevertheless, the obtained NP diameter of 268 nm is still considered an excellent result (6,35% relative error).

Furthermore, after calculating the area under each population, we discovered that the one centered at 268 nm had a bigger area compared to the one centered at 500 nm. However, these areas were in a 1,46 ratio, which is very similar to the concentration ratio of the NPs. This shows that the probability of the particle passing through the pore is proportional to its concentration, and mixing did not seem to influence it in the given range.

By analyzing the results of the mixing study, we concluded that the study was successful. The PDMS devices can resolve the spike populations caused by different particles while still being accurate and precise. This meant that we could try more complex samples such as human serum and purified EVs.

4.2.8 Biological Experiments

4.2.8.1 Human Serum

Human blood is made of a complex mixture of small molecules and many types of cells, such as red and white blood cells. The serum is extracted from whole blood right after clotting and removing cells and some proteins. The obtained serum primarily consists of a broad size range of proteins, EVs, and hemoglobin [38].

Due to the broad size range of the contents of the sample and to test the ability of the devices to analyze more complex samples, human serum was used in two different chip Designs. We tested this biological sample on Design 2 (W=600nm) and Design 5 (W=1000nm). Designs 2 has single constriction nanochannels, and Design 5 has no constrictions (smooth pore). No double constriction channels were used in this study.

As mentioned above, serum mainly consists of proteins, but it also has other molecules, such as cholesterol, triglycerides, and glucose. Therefore, we focused on the total protein concentration to make dilutions on 137 mM NaCl PBS (Table 17).

Table 17 – Serum fraction present in the solutions used with the corresponding total protein concentration.

Serum fraction	Protein Concentration (g/mL)
100%	0,052
50%	0,026

Initially, the solutions with a 50% serum fraction were tested on the two chosen designs. In Figure 12 are examples of the data collected from each chip design. It is not represented, but as these devices worked with a 50% serum fraction, we tested Design 5 for 100% serum solutions and those experiments were also successful. The corresponding Raw Data and Relative Current Amplitude shift histograms of the data represented in Figure 12 are in section 7.10.1 of the Supporting Information. It is also important to highlight that when running the serum experiments, the baseline had a different behavior than what we were used to during the experiments on standard particles.

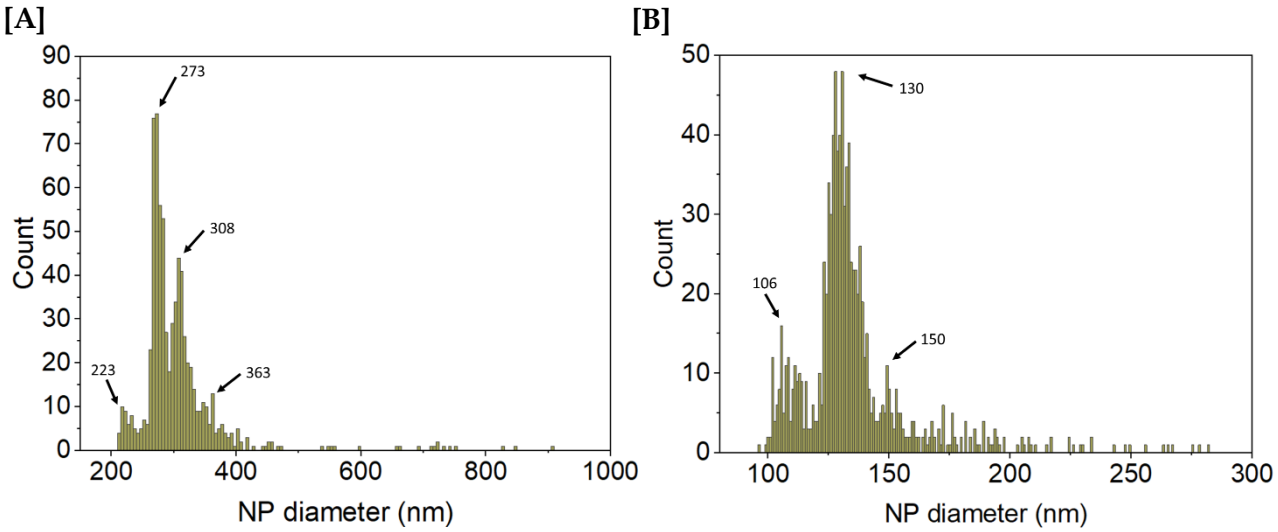

Figure 12 – Histograms of the Expected NP diameter of the human serum sample in [A] Design 5 (W=1000 nm)for 100 and 150 mbar, and [B] Design 2 (W=600 nm) with only applying 150 mbar. The identified populations are marked by black arrows.

As in the NP mix study (section 4.2.7), we used the same equation described to transform the Relative Amplitude shift into the Expected NP diameter. For each design, there were at least 3 populations identified. These populations represent the most common size of the biological particles that passed through the pore. The biggest population for Design 5 was 273 nm (Figure 12A) and 130 nm for Design 2 (Figure 12B).

According to literature, 140 nm-sized EVs can be found in human serum after purification in a concentration of 2,3 x 10^9 particles/mL [39]. This size matches the population identified with Design 2, which makes the characterization of EVs using microfluidic devices very promising.

Thus, with all the information obtained, we estimated that the sample had a biological content ranging from 106 to 363 nm and that the biological particles with 273 nm were present in higher concentration than all the other populations.

Of all the designs used to study the human serum sample, Design 5 had the biggest detecting range. The device identified 4 populations and they were within a 140 nm interval, which is 3 times bigger than the detection interval of Design 2. However, it did not detect the biological particles with a size below 200 nm, unlike Design 2.

This study just shows that it is possible for the PDMS devices to register spikes from biological origins and characterize the sample. Also, regarding the analysis of a sample that has a broad size range of components a wider nanochannel design seems to be more suitable.

4.2.8.2 Purified EVs

To further understand how the fabricated PDMS devices handle biological samples, we tested them with a purified sample of EVs. In this study, we used Design 2 (W=600nm) and Design 5 (W=1000nm). The EVs provided to us were isolated from HCT116 colon cancer cells by ultracentrifugation and resuspended in dPBS with a concentration of 1x10^9 to 2x10^9 particles/mL. This concentration was the desired one according to our Concentration Study (section 4.2.6) and no dilutions were made.

As in our other biological experiments, we focused on the current amplitude shift caused by the passing of a particle through the nanopore and transformed that data into the expected NP diameter (Figure 13). This sample was characterized with DLS by INL collaborators beforehand. The obtained size distribution is in section 7.10.2 of the Supporting Information. The purified EVs sample had three populations centered at 159, 316 and 424 nm, previously identified by the collaborators of the project. However, the bump in the distribution centered at 230 nm was considered as a fourth population.

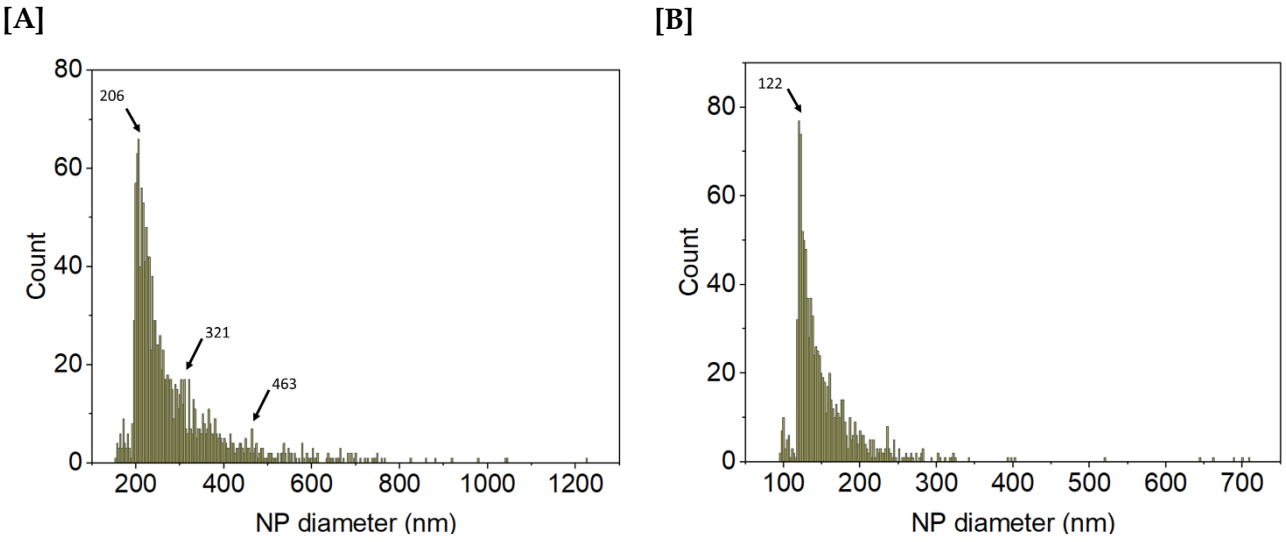

Figure 13 – Histograms of the Expected NP diameter of the purified EVs sample in [A] Design 5 and [B] Design 2. The identified populations are marked by black arrows. The spikes in Design 5 were registered with 150 mbar, while in Design 2 it was applied 100 and 150 mbar.

As shown in the histograms of Figure 13, Design 5 (Figure 13A) detects Extracellular Vesicle populations that have a bigger size, corresponding approximately to three populations identified beforehand (230, 316 and 424 nm). The populations identified using Design 5 all have relative errors close to or below 10%. The height of the populations matches the concentration obtained for those populations on the analysis made by the collaborators. On the other hand, Design 2 (Figure 13B) could only identify one population related to the 159 nm one but with a higher relative error of 30%. This indicates that Design 2 is better for the characterization of smaller EVs, while Design 5 can easily identify populations above 200 nm in diameter.

These results show that the produced PDMS devices are reliable for the characterization of any biological sample, as they can successfully identify size populations in the sample and give an idea of their concentration.

4.2.9 Patch-Clamp Amplifier vs. RPS Interface

As mentioned in the beginning, the equipment used to perform the RPS measurements was Patch-Clamp Amplifier. This equipment is usually used to measure electrical current in brain cells; however, it is a very complex and expensive instrument. Therefore, there is a need to develop cost-effective and more practical instrumentation. To achieve this, INL researchers developed an In-house made RPS Interface. In section 7.11 of the Supporting Information, we will compare the signal performance of the RPS interface with Patch-Clamp, to gather useful information for the development of future instrumentation.

5 Conclusions and Future Perspectives

We started this project by using one type of nanopore: glass nanopipettes. However, we soon realized that the equipment available to us to fabricate these was not the most suitable. As we could not overcome this issue, we focused this project on studying chip-based nanopores.

We had six chip designs available to us with different geometries. The main difference between the devices was the nanochannel type, as it could have either a smooth, single, or double constriction channel. To test the ability of these chip-based nanopores to detect particles, we used pressure-driven resistive-pulse sensing to measure current spikes, when these particles moved through the pore.

After almost 400 experiments performed and 300 PDMS devices used, we determined which combinations of design and NP could successfully register spikes for high and low concentration solutions. Further studies on the relative amplitude of these spikes led to 12 good combinations: Design 2 with 230 nm NPs, Design 2 with 252 nm NPs, Design 5 with 252 nm NPs, Design 5 with 500 nm NPs, Design 7 with 500 nm NPs and Design 12 with 500 nm NPs, all for both high and low NP concentrations. Out of all these good combinations, Design 5 presents the highest accuracy and precision compared to the other good designs.

As we did these experiments, we analyzed how the pulse shape is influenced by pressure-driven flow. Thus, we were able to identify common behaviors across the devices and categorized them as "ideal", "working", and "non-working". In the ideal measurements, the amplitude of the spikes is not significantly affected by the pressure applied, but the width of the spikes is, as it decreases with increasing pressure, indicating the particles become faster.

We also showed that particle movement is ruled by pressure-driven transport and not electrical transport by theoretical calculations. Such conclusions are further confirmed because different designs have similar spike widths for the same pressure applied, no matter the particle size.

Regarding the concentration study, we found that we got better results for concentrations ranging from 10^8 to 10^9 particles/mL. These concentrations allow us to register the optimal quantity of spikes for analysis. It is also important to note that our devices have a detection limit of 10^7 particles/mL, which results from the frequency "rule" established at the beginning.

Lastly, we confirmed that chip-based nanopores could register biological spikes and accurately characterize samples of biological origin, such as human serum and purified EVs, using pressure-driven resistive-pulse sensing. These findings are helpful to understand the possibilities of potential applications of RPS in the characterization and analysis of EVs.

The results of the many studies performed led us to conclude that Design 5 is the most suitable design for the characterization and size estimation of model NPs and Extracellular Vesicles. Even though more complex designs were tested, with single and double constriction channels, our findings show that a smooth channel with no constrictions gives more accurate and reliable results.

In the next steps of this project, it would be interesting to use smaller NPs or channels. In terms of mixing study, this means makings a mixture of particles from 100 to 500 nm in a size range to test how microfluidic devices distinguish and characterize smaller model particles mixed with bigger ones, to further investigate limitations on channel size vs. particle diameter. Regarding biological samples, the purified EVs sample could be characterized with a smaller channel to better understand how channel size can influence results, especially to confirm if EVs are lost in the noise signal. Another interesting aspect of studying biological samples would be to spike a human serum sample with EVs, characterize it using Design 5, and investigate if the populations match the expected ones.

6 References

[1] H. P. T. Nguyen, R. J. Simpson, L. A. Salamonsen, and D. W. Greening, “Extracellular vesicles in the intrauterine environment: Challenges and potential functions,” *Biol. Reprod.*, vol. 95, no. 5, pp. 1–12, Nov. 2016, doi: 10.1095/biolreprod.116.143503.

[2] I. S. Batth *et al.*, “Circulating tumor markers: harmonizing the yin and yang of CTCs and ctDNA for precision medicine.,” *Ann. Oncol. Off. J. Eur. Soc. Med. Oncol.*, vol. 28, no. 3, pp. 468–477, Mar. 2017, doi: 10.1093/annonc/mdw619.

[3] J. Weng *et al.*, “Extracellular vesicles, the cornerstone of next-generation cancer diagnosis?,” *Semin. Cancer Biol.*, May 2021, doi: 10.1016/j.semcancer.2021.05.011.

[4] L. Doyle and M. Wang, “Overview of Extracellular Vesicles, Their Origin, Composition, Purpose, and Methods for Exosome Isolation and Analysis,” *Cells*, vol. 8, no. 7, p. 727, Jul. 2019, doi: 10.3390/cells8070727.

[5] S. EL Andaloussi, I. Mäger, X. O. Breakefield, and M. J. A. Wood, “Extracellular vesicles: biology and emerging therapeutic opportunities.,” *Nat. Rev. | Drug Discov.*, vol. 12, no. 5, pp. 347–357, May 2013, doi: 10.1038/nrd3978.

[6] A. Kerviel, M. Zhang, and N. Altan-Bonnet, “A New Infectious Unit: Extracellular Vesicles Carrying Virus Populations,” *Annu. Rev. Cell Dev. Biol.*, vol. 37, no. 1, pp. 171–197, Oct. 2021, doi: 10.1146/annurev-cellbio-040621-032416.

[7] K. M. Candelario and D. A. Steindler, “The role of extracellular vesicles in the progression of neurodegenerative disease and cancer.,” *Trends Mol. Med.*, vol. 20, no. 7, pp. 368–74, Jul. 2014, doi: 10.1016/j.molmed.2014.04.003.

[8] S. Maacha *et al.*, “Extracellular vesicles-mediated intercellular communication: roles in the tumor microenvironment and anti-cancer drug resistance.,” *Mol. Cancer*, vol. 18, no. 1, p. 55, Dec. 2019, doi: 10.1186/s12943-019-0965-7.

[9] S. Guo, S. Tao, and H. Dawn, “Microfluidics-based on-a-chip systems for isolating and analysing extracellular vesicles,” *J. Extracell. Vesicles*, vol. 7, no. 1, 2018, doi: 10.1080/20013078.2018.1508271.

[10] E. Reátegui *et al.*, “Engineered nanointerfaces for microfluidic isolation and molecular profiling of tumor-specific extracellular vesicles.,” *Nat. Commun.*, vol. 9, no. 1, p. 175, Dec. 2018, doi: 10.1038/s41467-017-02261-1.

[11] M. Monguió-Tortajada, C. Gálvez-Montón, A. Bayes-Genis, S. Roura, and F. E. Borràs, “Extracellular vesicle isolation methods: rising impact of size-exclusion chromatography.,” *Cell. Mol. Life Sci.*, vol. 76, no. 12, pp. 2369–2382, Jun. 2019, doi: 10.1007/s00018-019-03071-y.

[12] S. Gholizadeh *et al.*, “Microfluidic approaches for isolation, detection, and characterization of extracellular vesicles: Current status and future directions,” *Biosens. Bioelectron.*, vol. 91, pp. 588–605, May 2017, doi: 10.1016/j.bios.2016.12.062.

[13] J. Hardij *et al.*, “Characterisation of tissue factor-bearing extracellular vesicles with AFM: comparison of air-tapping-mode AFM and liquid Peak Force AFM.,” *J. Extracell. vesicles*, vol. 2, no. 1, p. 21045, Jan. 2013, doi: 10.3402/jev.v2i0.21045.

[14] Y. Liu *et al.*, “Sizing Single Particles at the Orifice of a Nanopipette,” *ACS Sensors*, vol. 5, no. 8, pp. 2351–2358, Aug. 2020, doi: 10.1021/acssensors.9b02520.

[15] D. Buschmann, V. Mussack, and J. B. Byrd, “Separation, characterization, and standardization of extracellular vesicles for drug delivery applications,” *Adv. Drug Deliv. Rev.*, vol. 174, pp. 348–368, Jul. 2021, doi: 10.1016/J.ADDR.2021.04.027.

[16] L. Chen *et al.*, “Millifluidics, microfluidics, and nanofluidics: manipulating fluids at varying length scales,” *Mater. Today Nano*, vol. 16, p. 100136, Dec. 2021, doi: 10.1016/J.MTNANO.2021.100136.

[17] E. I. Mancera-Andrade *et al.*, “Isorhamnetin encapsulation into biogenic silica from Cyclotella sp. using a microfluidic device for drug delivery applications,” *Biocatal. Agric. Biotechnol.*, vol. 19, p. 101175, May 2019, doi: 10.1016/j.bcab.2019.101175.

[18] M. L. S. Silva, “Microfluidic devices for glycobiomarker detection in cancer,” *Clin. Chim. Acta*, vol. 521, pp. 229–243, Oct. 2021, doi: 10.1016/j.cca.2021.07.013.

[19] S.-B. B. Cheng, M.-M. M. Chen, Y.-K. K. Wang, Z.-H. H. Sun, M. Xie, and W.-H. H. Huang, “Current techniques and future advance of microfluidic devices for circulating tumor cells,” *TrAC Trends Anal. Chem.*, vol. 117, pp. 116–127, Aug. 2019, doi: 10.1016/j.trac.2019.06.018.

[20] K. Kant *et al.*, “Microfluidic devices for sample preparation and rapid detection of foodborne pathogens.,” *Biotechnol. Adv.*, vol. 36, no. 4, pp. 1003–1024, Jul. 2018, doi: 10.1016/j.biotechadv.2018.03.002.

[21] V. Calero, “Electrokinetic biased Deterministic Lateral Displacement for particle separation,” University of Southampton, 2021.

[22] K. M. Weerakoon-Ratnayake, S. Vaidyanathan, C. A. Amarasekara, C. K. Johnson, and S. A. Soper, “Single molecule analysis in nanofluidic devices,” in *Spectroscopy and Dynamics of Single Molecules*, Elsevier, 2019, pp. 335–377.

[23] A. J. Shnoudeh *et al.*, “Synthesis, Characterization, and Applications of Metal Nanoparticles,” in *Biomaterials and Bionanotechnology*, Elsevier, 2019, pp. 527–612.

[24] B. Gas, “ELECTROPHORESIS | Principles,” in *Encyclopedia of Analytical Science*, 2nd Editio., Elsevier, 2005, pp. 363–370.

[25] D. Stein, M. G. L. van den Heuvel, and C. Dekker, “Chapter 1. Transport of Ions, DNA Polymers, and Microtubules in the Nanofluidic Regime,” in *Nanofluidics: Nanoscience and Nanotechnology*, First., J. B. Edel and A. J. DeMello, Eds. The Royal Society of Chemistry, 2008, pp. 1–30.

[26] A. Ainla, “The Multifunctional Pipette. A Microfluidic Technology for the Biosciences.,” Chalmers University of Technology, 2013.

[27] O. D. Neikov and N. A. Yefimov, “Powder Characterization and Testing,” in *Handbook of Non-Ferrous Metal Powders*, Elsevier, 2019, pp. 3–62.

[28] L. Yang and T. Yamamoto, “Quantification of Virus Particles Using Nanopore-Based Resistive-Pulse Sensing Techniques,” *Front. Microbiol.*, vol. 7, no. SEP, Sep. 2016, doi: 10.3389/fmicb.2016.01500.

[29] D. G. Haywood, A. Saha-Shah, L. A. Baker, and S. C. Jacobson, “Fundamental studies of nanofluidics: Nanopores, nanochannels, and nanopipets,” *Analytical Chemistry*, vol. 87, no. 1. pp. 172–187, Jan. 06, 2015, doi: 10.1021/ac504180h.

[30] M. Karhanek, J. T. Kemp, N. Pourmand, R. W. Davis, and C. D. Webb, “Single DNA molecule detection using nanopipettes and nanoparticles.,” *Nano Lett.*, vol. 5, no. 2, pp. 403–7, Feb. 2005, doi: 10.1021/nl0480464.

[31] Y. Wang, D. Wang, and M. V. Mirkin, “Resistive-pulse and rectification sensing with glass and carbon nanopipettes,” *Proc. R. Soc. A Math. Phys. Eng. Sci.*, vol. 473, no. 2199, p. 20160931, Mar. 2017, doi: 10.1098/rspa.2016.0931.

[32] N. Vogel *et al.*, “Color from hierarchy: Diverse optical properties of micron-sized spherical colloidal assemblies.,” *Proc. Natl. Acad. Sci. U. S. A.*, vol. 112, no. 35, pp. 10845–50, Sep. 2015, doi: 10.1073/pnas.1506272112.

[33] S.-B. Cheng *et al.*, “Three-Dimensional Scaffold Chip with Thermosensitive Coating for Capture and Reversible Release of Individual and Cluster of Circulating Tumor Cells.,” *Anal. Chem.*, vol. 89, no. 15, pp. 7924–7932, Aug. 2017, doi: 10.1021/acs.analchem.7b00905.

[34] P. Terejánszky, S. Papp, S. Berényi, and R. E. Gyurcsányi, “Resistive Pulse Sensing as a High-Resolution Nanoparticle Sizing Method: A Comparative Study,” *Part. Part. Syst. Charact.*, vol. 36, no. 6, p. 1800543, Jun. 2019, doi: 10.1002/ppsc.201800543.

[35] L. Lastra *et al.*, “The Origin of Conductive-Pulse Sensing Inside a Nanopore and the Role of Electro-Hydrodynamics,” *bioRxiv Biophys.*, pp. 1–20, 2020, doi: 10.1101/2020.09.25.310755.

[36] W. Hellmich, J. Regtmeier, T. T. Duong, R. Ros, D. Anselmetti, and A. Ros, “Poly(oxyethylene) based surface coatings for poly(dimethylsiloxane) microchannels.,” *Langmuir*, vol. 21, no. 16, pp. 7551–7, Aug. 2005, doi: 10.1021/la0510432.

[37] W. Koehrsen, “The Poisson Distribution and Poisson Process Explained,” *Towards Data Science*, Jan. 2019. https://towardsdatascience.com/the-poisson-distribution-and-poisson-process-explained-4e2cb17d459 (accessed Nov. 25, 2021).

[38] A. C. Dona, “High-Throughput Metabolic Screening,” in *Metabolic Phenotyping in Personalized and Public Healthcare*, E. Holmes, J. K. Nicholson, A. W. Darzi, and J. C. B. T.-M. P. in P. and P. H. Lindon, Eds. Boston: Elsevier, 2016, pp. 111–136.

[39] S. Chen *et al.*, “Lipidomic characterization of extracellular vesicles in human serum.,” *J. Circ. biomarkers*, vol. 8, p. 1849454419879848, Jan. 2019, doi: 10.1177/1849454419879848.

[40] A. Oesterle, “Pipette Cookbook,” *Sutter Instrument Company*, 2018. https://www.sutter.com/PDFs/pipette_cookbook.pdf (accessed Oct. 02, 2021).

[41] E. Joseph and G. Singhvi, “Multifunctional nanocrystals for cancer therapy: a potential nanocarrier,” in *Nanomaterials for Drug Delivery and Therapy*, Elsevier, 2019, pp. 91–116.

7 Supporting Information

7.1 Nanopipette fabrication and characterization

The pipette puller model used has a filament as a heating element to melt the glass. The experiments were performed in Time mode, meaning that all measurements were done with the default Pressure setting (500 units). To create a recipe, four parameters were inserted into the machine: Heat, Pull, Velocity and Time.

The Heat is the amount of current delivered to the filament. It does not represent temperature. This value is dependent on the dimensions of the capillaries as the filament needs to get hot enough to melt the glass. Therefore, the actual Heat value needs to be determined for that specific batch of capillaries before anything else. This is called a Ramp Test. The Pull parameter is the hard pull applied after the glass is soft enough. In cases where the Pull is 0, this means that the plunger of the machine is used to pull on the glass. The Velocity indicates when the Heat is turned off, and the cooling process starts. The Time determines the duration of the cooling of the glass and the filament when the capillary is being pulled. A Time value of 250 corresponds to 125 ms. The Loop parameter indicates how many times the machine should loop over that line of programming. As we used model P-97, this number indicates how many lines of programming were inserted in the machine. The looping can stop before the number is reached if the glass capillary breaks [40].

Multiple combinations of parameters were done to get pipettes with different IDs, but the most relevant ones are in Table 18.

Table 18 – Parameters used that got the most relevant results.

Recipe	Heat	Pull	Velocity	Time	Loop
1	549	0	50	250	3
2	549	0	70	250	3

7.1.1 Nanopipette pulling

As mentioned in section 3.1 of the Materials and Methods, the pipettes were pulled using a Micropipette Puller. After turning it on, the desired parameters were inserted into the machine. The glass capillaries were inserted in the holds making sure they passed through the filament holes without touching them. Then, the program was started. When the filament is heating the capillary, it lights up. As soon as the capillary is melted in half and transformed into two pipettes, the holds instantly move from the filament (Figure 14).

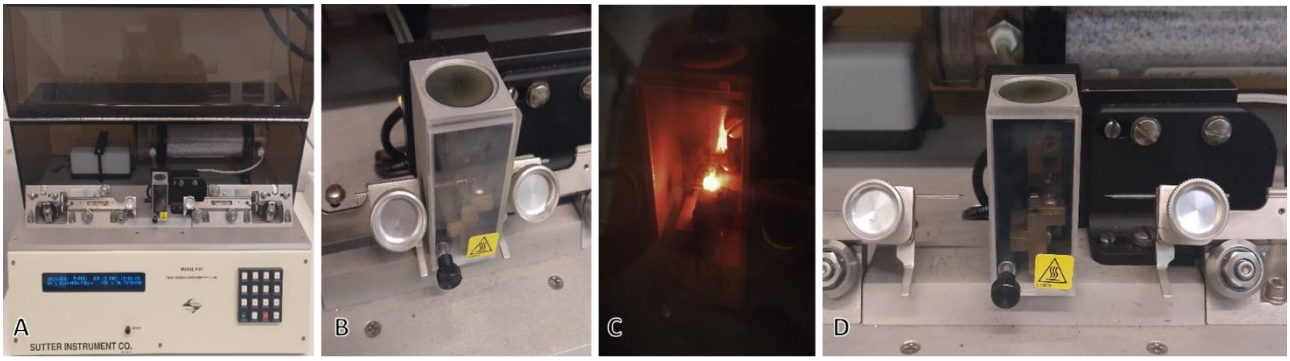

Figure 14 – Step by step images of the nanopipette pulling process: (A) the pipette puller machine, (B) glass capillary going through the filament, (C) the heating of the capillary, and (D) the transformation of the glass capillary into two pipettes.

7.1.2 Nanopipette characterization

The nanopipettes were characterized by SEM, using a 10 kV accelerating voltage. The images taken are displayed in (Figure 15).

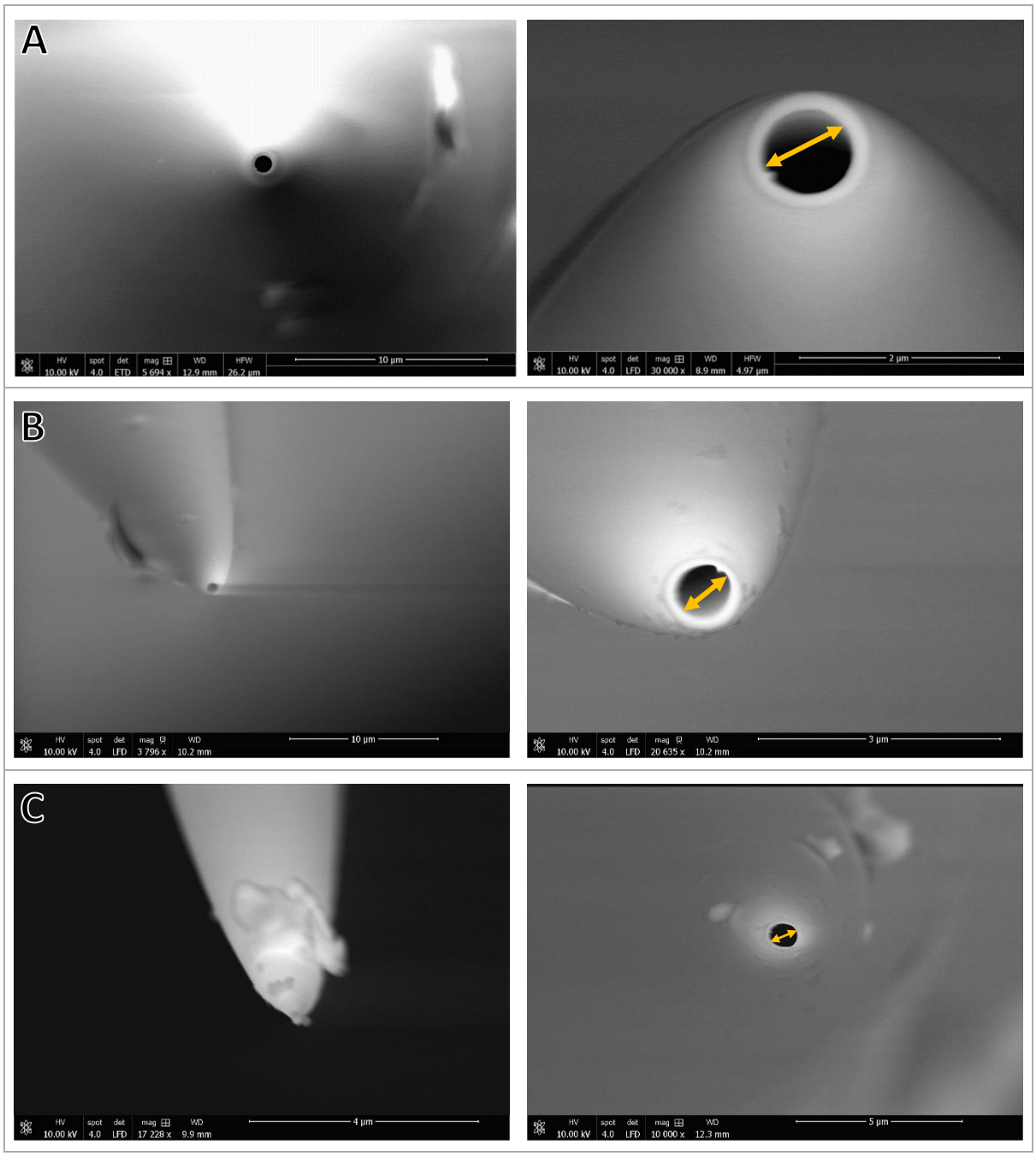

Figure 15 – SEM images of the pulled nanopipettes: (A) Pipette A, (B) Pipette B, and (C) Pipette C. Marked in yellow is the place where the ID measurements were taken.

7.2 Optical Microscope Images

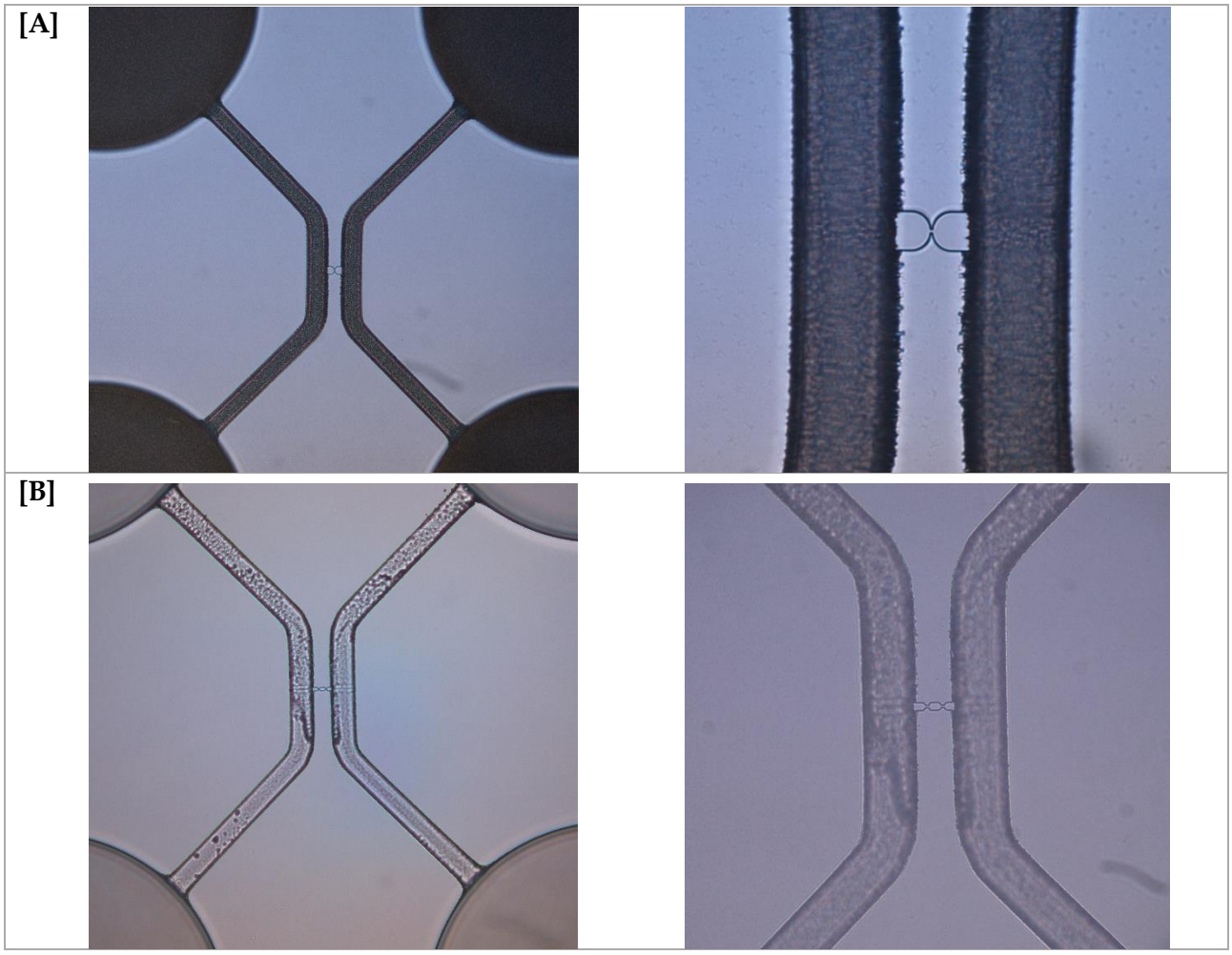

Figure 16 – Images captured with an Optical Microscope of [A] Design 7 and [B] Design 12.

7.3 Nanoparticle concentration conversion

To properly quantify the particles being inserted in the devices, the concentration of the solution was converted from g/mL to particles/mL. To achieve that, we established a relationship between the total volume occupied by the particles and one single particle (Eq. 12). Here we considered a particle as a perfect sphere.

$$\frac{total\ volume}{NP\ volume} = \frac{m}{\rho_d}\Big/\left(\frac{4}{3}\times\pi\times\left(\frac{d}{2}\right)^3\right) = \frac{C\times V}{\rho_d}\Big/\left(\frac{4}{3}\times\pi\times\left(\frac{d}{2}\right)^3\right)$$
$$= \frac{C}{\rho_d}\Big/\left(\frac{4\pi\times d^3}{24}\right) = \frac{6C}{\rho\times\pi\times d^3}\left(\frac{particles}{mL}\right) \quad (12)$$

where C is the solution concentration in g/mL (2% solids translates into 0.02 g/mL), d is the diameter of the NP in cm^3, and ρ_d is the density of the particles in g/cm^3. As all the NPs used were polystyrene beads (ρ = 1,05 g/cm^3), Eq. 12 can be modified to:

$$\frac{6C}{\rho\times\pi\times d^3} \Rightarrow \frac{6C}{1{,}05\pi\times d^3}\ (particles/mL) \quad (13)$$

7.4 Dynamic Light Scattering Results

DLS can be used to determine the zeta potential of NPs. A zeta potential between -30 mV and +30 mV is not ideal, as it is considered to represent particles that do not have sufficient repulse force to maintain the stability of the solution [41]. In Table 19 are the zeta potential values obtained, and they are within the not ideal threshold, and even though the values are closer to -30 than 0, it means that the NPs will have some tendency to aggregate.

Table 19 – Average of the measured Zeta Potential for each NP.

NP diameter (nm)	Zeta Potential Mean (mV)
230	-16,33 ± 7,24
252	-19,17 ± 5,99
500	-15,33 ± 2,55

7.5 Nanopipette Patch-Clamp schematic

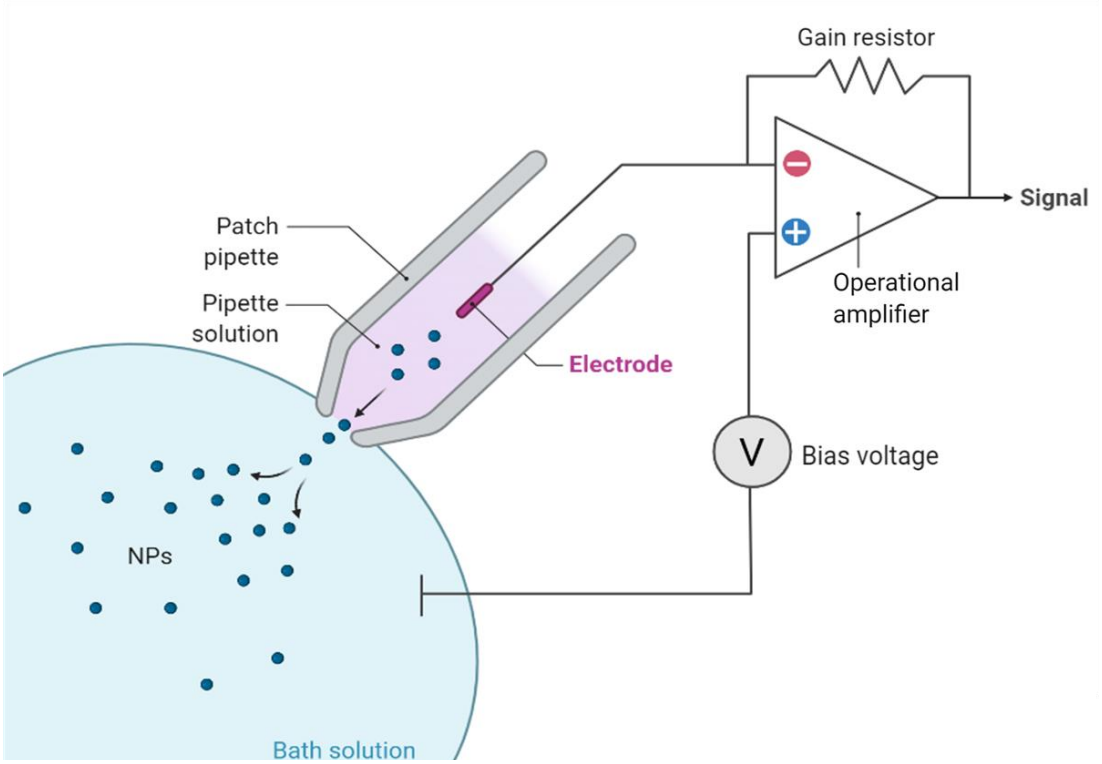

Figure 17 – Patch-Clamp schematic of experiments on glass nanopipettes. Adapted from "Patch-Clamp Recording Principle", by BioRender.com (2021). Retrieved from https://app.biorender.com/biorender-templates

7.6 Nanopipette Cone Resistance

The calculation of the resistance of the cone is more complex. Therefore, we considered that the radius of the cone decreases linearly, and it can be written in function of x.

$$r(x) = \frac{r - \frac{ID}{2}}{L}x + \frac{ID}{2} \Longrightarrow A(x) = \pi[r(x)]^2 = \pi\left(\frac{r - \frac{ID}{2}}{L}x + \frac{ID}{2}\right)^2$$

$$R_\Delta = \rho\frac{L}{A} \Rightarrow dR = \rho\int\frac{dx}{A(x)}$$

$$R_\Delta = \rho \int \frac{dx}{\pi\left(\frac{r-\frac{ID}{2}}{L}x+\frac{ID}{2}\right)^2} = \frac{1}{\sigma\pi}\int_0^L \frac{dx}{\left(\frac{r-\frac{ID}{2}}{L}x+\frac{ID}{2}\right)^2}$$

$$= -\frac{1}{\sigma\pi}\left(\frac{r-\frac{ID}{2}}{L}\right)^{-1}\left(\frac{1}{r}-\frac{2}{ID}\right) = \frac{2L_2}{\sigma\pi rID}$$

7.7 Nanopipette Particle Detection Results

As mentioned in section 4.1.2 of the Glass Nanopipettes study, the minimal resistance change affects the ID of the pipette, influencing particle detection. In this section we will show the exact results obtained for the two examples mentioned in 4.1.2.

In Figure 18 we have the raw current data. We can observe that there is a significant drop in the current baseline, caused by the clogging of the nanopipette by the nanoparticles used.

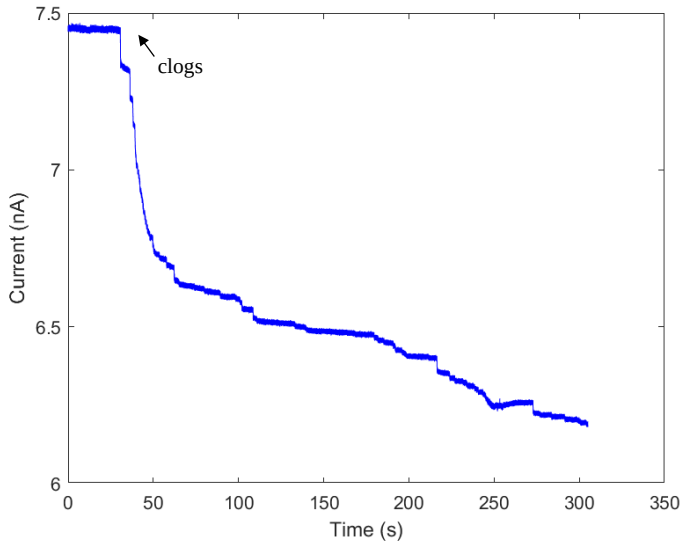

Figure 18 – Baseline current over time for Example 1.

In the case of Figure 19, we have the resulting current graph for the successful Example 2. At the start the current saturated but as time went by and due to a pressure change it stabilized, and we got spikes. This happened because there was something blocking the orifice of the pipette that got loose with the increase of pressure. Even though the experiment lasted almost 8 minutes, we only could get spikes for a short period. This results from the clogging of the pipette caused by the considerable number of particles going through the orifice of the pipette. This is what causes the significant current drop right after the registered spikes (marked in red).

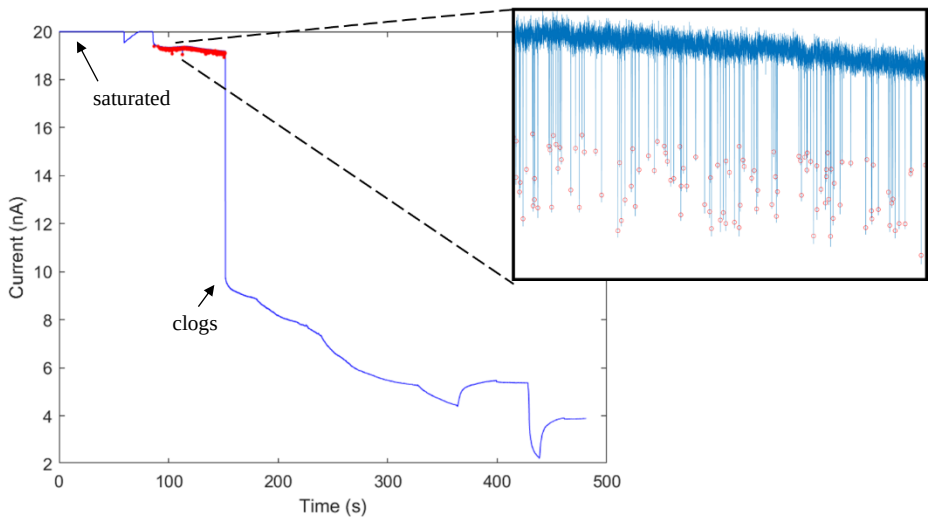

Figure 19 – Current graphs for Example 2. The detected spikes are marked in red.

In Table 20 we have the summary of the obtained values for the different parameters after analyzing the spikes. As only one pressure section had spikes, it is not even possible to study the pressure dependence.

Table 20 – Specific parameter values obtained from the analyzes of the spikes.

Pressure (mbar)	Number of Spikes	Amplitude (pA)	Amplitude Shift (%)	Width (ms)
50	1216	87,49 ± 21,35	0,45 ± 0,11	0,35 ± 0,04

7.8 Examples of the categorized behaviors

A

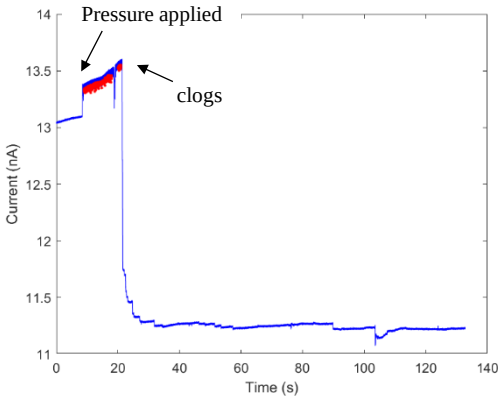

Working: One data point only.

Obeys the frequency rule. The chip got clogged when the pressure was increased. Baseline became stable but no more spikes.

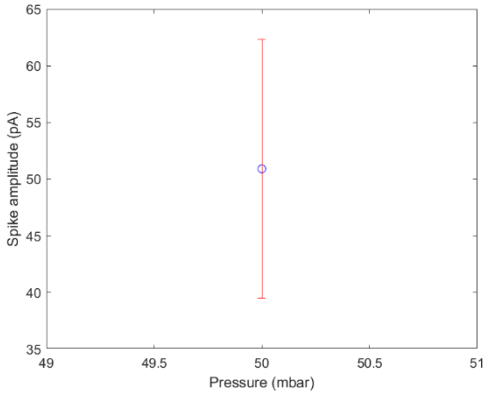

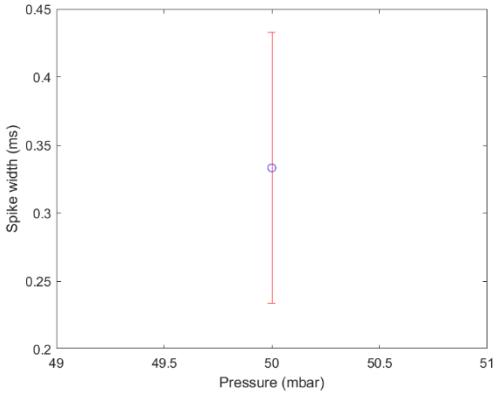

B

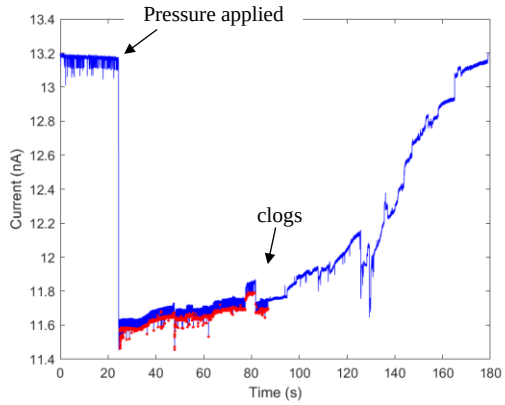

Working: Device clogs suddenly and there are no more spikes (or only a few) after that.

The chip gets clogged after the registered spikes and baseline becomes unstable. The width of the spikes increases until it clogged.

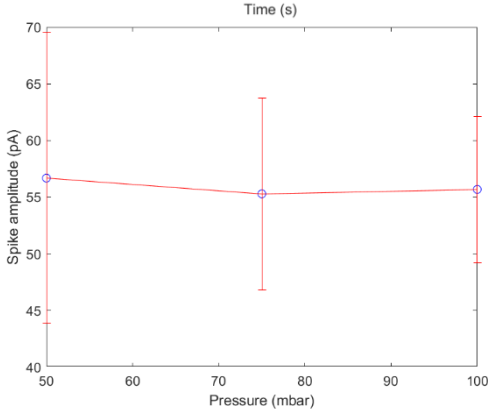

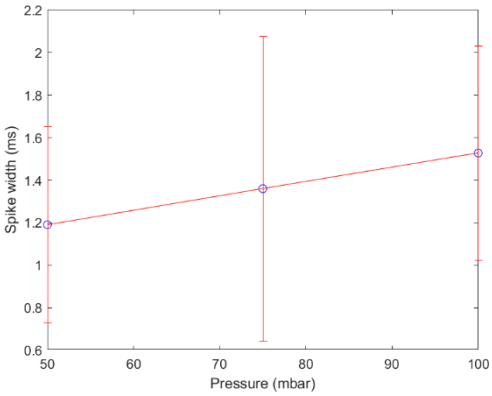

C

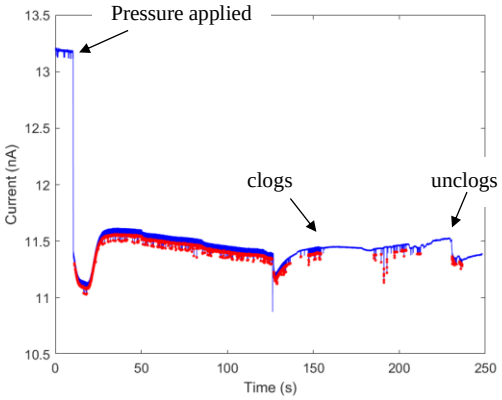

Working: Device clogs suddenly but unclogs at the end of the experiment.

The spikes between the clog and unclogging of the device were discarded, as they were too broad. Probably result from the process of unclogging.

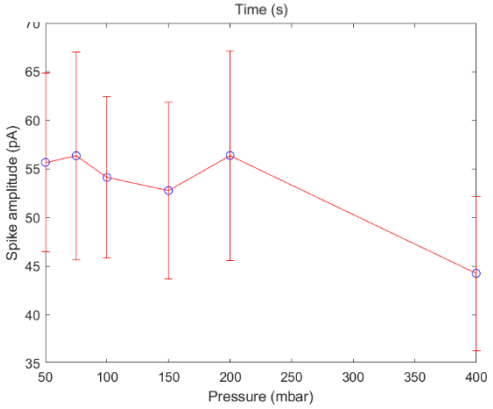

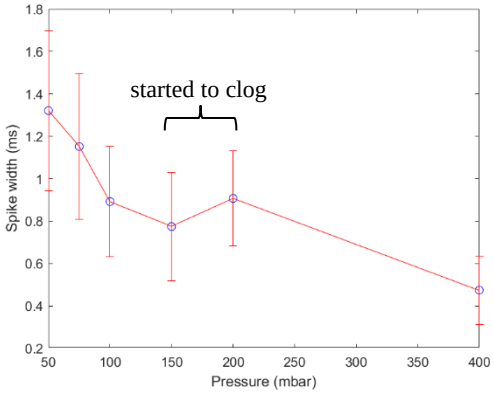

D

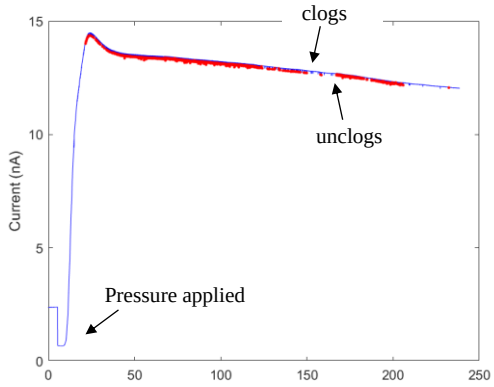

Working: Device clogs suddenly but unclogs straight away.

The baseline was stable.

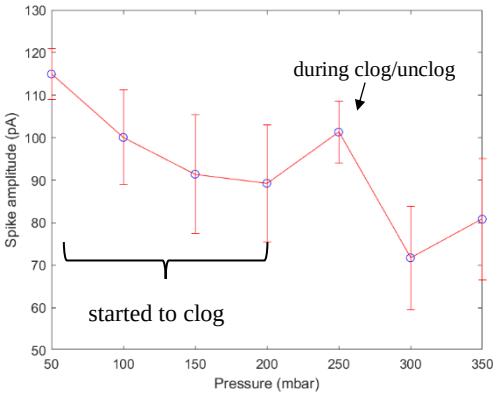

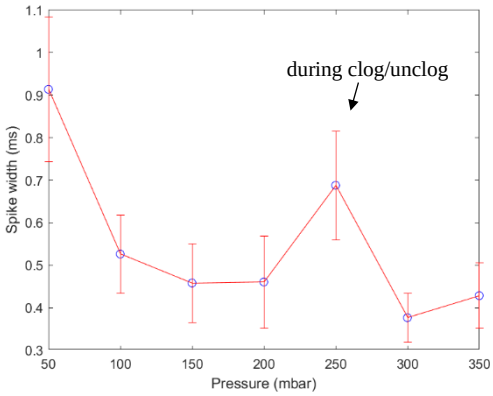

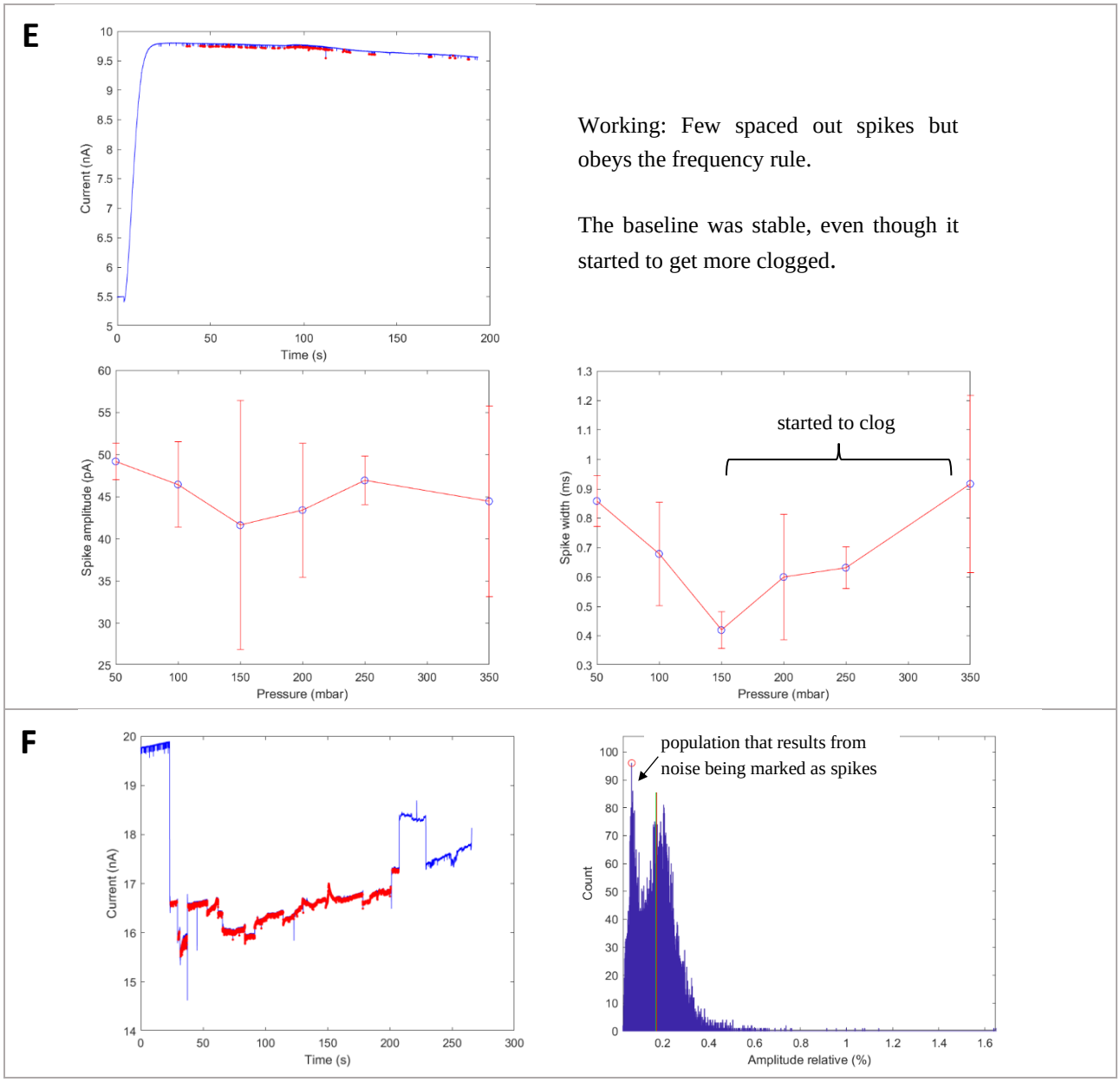

Figure 20 – Working device graphs for the identified behaviors: [A] one data point only, all the sudden clogging variations ([B], [C], [D]), [E] few spikes but obeys the frequency rule, [F] unstable baseline. The data sets from [A] to [E] have three graphs: raw data, spike amplitude vs. pressure applied, and spike width vs. pressure applied. The last data set [F] has the raw data and the histogram of the relative amplitude shift. The spikes registered are marked in red in the raw data graph.

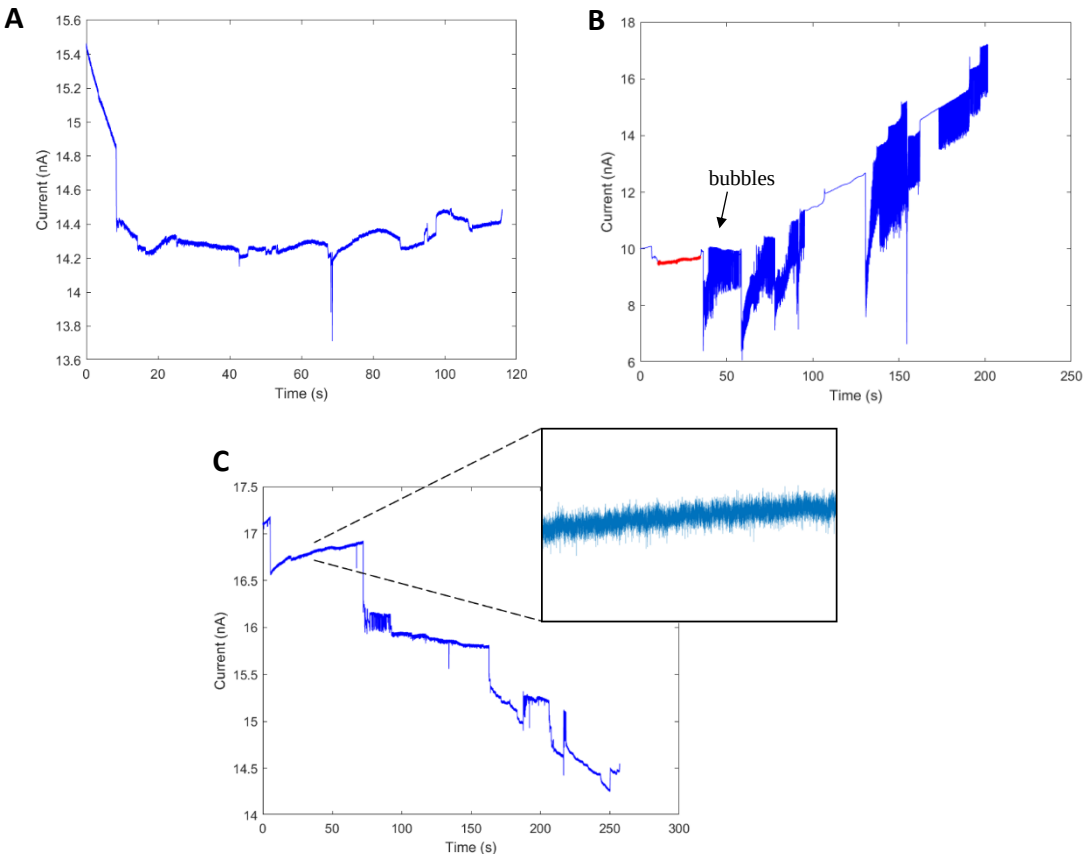

Figure 21 – Raw data of the non-working devices for the identified behaviors: [A] No spikes, [B] Many bubbles going through the pore after a few spikes and clogging, and [C] too much noise.

7.9 Theoretical values and equations

7.9.1 Electrical Resistance

The total electrical resistance is the microfluidic device is given by:

$$R_{total} = R_{nano} + R_{micro} + R_{macro} \tag{14}$$

where R_{nano} is the resistance of the nanochannel, R_{micro} the resistance of the microchannels, and R_{macro} the resistance of the macrochannels. The resistance of the micro and macrochannels were calculated with the following equations:

$$R_{micro} = 2\left(\frac{L_A}{W_A H_A \sigma} + \frac{L_B}{W_B H_B \sigma}\right) \tag{15}$$

$$R_{macro} = \frac{2L}{WH\sigma} \tag{16}$$

where σ is the conductivity of PBS. The conductivity of PBS for a low salt solution is 1,46 S/m and 3,45 S/m for high salt solution. The dimensions and results of each equation are in Table 21.

Table 21 – Resistance of the macro and microchannels for low and high salt solutions.

		W (m)	***L*** (m)	***H*** (m)	**Resistance** (MΩ)	
					LS	HS
Macrochannels		3,0 x 10^{-4}	0,0057	1,5 x 10^{-5}	1,74	0,72
Micro-channels	Part A	2,0 x 10^{-5}	1,5 x 10^{-4}		0,91	0,38
	Part B	2,0 x 10^{-5}	4,9 x 10^{-5}			

Regarding the nanochannels resistance, it has 4 different components: the pore resistance (R_P), the connector resistance (R_C), the pre-connector resistance (R_{PC}), and, in the case of double constriction channels, the separation resistance (R_S). The R_{nano} results from the sum of all the components, and is calculated as follows:

$$R_{nano} = R_P + R_C + R_{PC} + R_S \tag{17}$$

Each component of the R_{nano} has its own equation. The resistance of the pore is given by:

$$R_P = \frac{L_P}{\sigma W_P H_P} \tag{18}$$

where L_P is the length of the pore, W_P the width of the pore and H_P the height of the pore. In the case of a double constriction channel Eq. 18 is transformed into:

$$R_P = \frac{2L_P}{\sigma W_P H_P} \tag{19}$$

The resistance of the connector results from an approximation as the cross sectional area of the connector decreases with the width from W_C to W_P. This resistance can be calculated as follows:

$$R_C = 2\left(\left(\frac{2}{\pi H_P \sigma}\right)\left(\ln\frac{W_C}{W_P}\right)\right) \tag{20}$$

where W_C is the width of the connector. In the case of a double constriction channel Eq. 20 is transformed into:

$$R_C = 4\left(\left(\frac{2}{\pi H_P \sigma}\right)\left(\ln\frac{W_C}{W_P}\right)\right) \quad (21)$$

The resistance of the pre-connector is given by the following equation:

$$R_{PC} = \frac{2L_{PC}}{\sigma W_{PC} H_{PC}} \quad (22)$$

where L_{PC}, W_{PC} and H_{PC} are the length, width, and height of the pre-connector, respectively. The resistance of the separation in double constriction channels is given by the following equation:

$$R_S = \frac{L_s}{\sigma W_S H_S} \quad (23)$$

where L_S, W_S and H_S are the length, width, and height of the separation, respectively. As these equations and dimensions all relate to nanochannels, the height of all components is 1 µm no matter the design. The other dimensions of the nanochannels are in Table 22.

Table 22 – Dimensions of all the nanochannel components.

	L_p (m)	W_P (m)	W_C (m)	L_{PC} (m)	W_{PC} (m)	L_s (m)	W_s (m)
Design 2	6,0 x 10^{-7}	5,0 x 10^{-7}	1,5 x 10^{-5}	-	-	-	-
Design 5	1,0 x 10^{-6}	1,5 x 10^{-5}	-	-	-	-	-
Design 7	6,0 x 10^{-7}	5,0 x 10^{-7}	7,5 x 10^{-6}	7,5 x 10^{-6}	3,52 x 10^{-4}	-	-
Design 11	5,0 x 10^{-7}	1,0 x 10^{-6}	3,0 x 10^{-6}	3,0 x 10^{-6}	2,51 x 10^{-6}	3,0 x 10^{-6}	2,01 x 10^{-6}
Design 12	1,0 x 10^{-6}	1,0 x 10^{-6}	3,0 x 10^{-6}	3,0 x 10^{-6}	3,51 x 10^{-6}	3,0 x 10^{-6}	2,01 x 10^{-6}
Design 13	5,0 x 10^{-7}	1,0 x 10^{-6}	3,0 x 10^{-6}	3,0 x 10^{-6}	5,05 x 10^{-6}	-	-

Using Table 22 and Eq. 18 to 23 we obtained the resistance of each component of the nanochannel. Then, using Eq. 17 we obtained the total nanochannel resistance. After that, with the initial Eq. 14 we calculated the total resistance for low and high salt solutions of each microfluidic device design (Table 23).

Table 23 – Resistance values for each component of the nanochannel and the total resistance.

		R_P (MΩ)	R_C (MΩ)	R_{PC} (MΩ)	R_S (MΩ)	R_{nano} (MΩ)	R_{Total} (MΩ)
Low salt (137 mM PBS)	Design 2	0,57	2,81	-	-	3,38	6,02
	Design 5	10,27	-	-	-	10,27	12,92
	Design 7	0,57	2,20	64,29	-	67,07	69,71
	Design 11	2,74	3,13	1,15	0,46	7,47	10,11
	Design 12	1,37	1,92	1,60	0,46	5,35	7,99
	Design 13	0,57	2,81	2,31	-	5,24	7,88
High salt (1 M PBS)	Design 2	0,24	1,17	-	-	1,41	2,51
	Design 5	4,29	-	-	-	4,29	5,39
	Design 7	0,24	0,92	26,82	-	27,98	29,08
	Design 11	1,14	1,30	0,48	0,19	3,12	4,22
	Design 12	0,57	0,80	0,67	0,19	2,23	3,33
	Design 13	0,57	0,65	0,96	-	2,19	3,29

7.9.2 Relative Current Amplitude Shift

The relative current amplitude shift is the parameter primarily used to analyze the data. It can be obtained using the relation between the resistance when there is a particle present in the microfluidic device and the total resistance of the system. This relation has an equation as follows:

$$I_{rel}\,(\%) = \left(\frac{R_{TP}}{R_{Total}} \times 100\right) - 100 \tag{24}$$

where R_{TP} is the total resistance of the system in the presence of a particle and R_{Total} is the total resistance of the system, already calculated in Table 23. The R_{TP} has many components as the R_{Total} mentioned in the previous section. However, the difference is the resistance in the pore when a particle is present. The total resistance of the system in the presence of a particle is similar to Eq. 14 and 17, and given by:

$$R_{TP} = R_{PP} + R_{micro} + R_{macro} + R_C + R_{PC} + R_S \tag{25}$$

where R_{PP} is the resistance of the pore when there is a particle present. This resistance depends on the geometry of the pore but also on the diameter of the particle moving through the pore, and follows the equation:

$$R_{PP} = \frac{1}{\sigma}\left(\frac{d}{(W_P - d)d + W_P(H_P - d)} + \frac{L_P - d}{W_P H_P}\right) \tag{26}$$

where d is the diameter of the NP. The results from Eq. 26, 25 and 24 are in Table 24 for each design and for both salt concentrations.

Table 24 – Relative current amplitude shift for each design according to which particle is present in the pore.

		R_{PP} (MΩ)		R_{TP} (MΩ)		I_{rel} (%)
		LS	HS	LS	HS	
230 nm	Design 2	0,60	0,25	6,05	2,52	0,4215
	Design 5	10,28	4,29	12,93	5,39	0,0681
	Design 7	0,60	0,25	69,74	29,09	0,0364
	Design 11	1,41	0,59	10,15	5,03	0,3686
	Design 13	1,41	0,59	7,92	3,30	0,4729
252 nm	Design 2	0,60	0,25	6,06	2,53	0,5653
	Design 5	10,29	4,29	12,93	5,39	0,0906
	Design 7	0,60	0,25	69,74	29,09	0,0488
	Design 11	1,42	0,59	10,16	5,04	0,4966
	Design 13	1,42	0,59	7,93	3,31	0,6371
500 nm	Design 2	0,98	0,41	6,43	2,68	6,7688
	Design 5	10,39	4,33	13,03	5,44	0,8837
	Design 7	0,98	0,41	70,12	29,25	0,5848
	Design 12	0,80	0,33	8,11	3,78	1,4285

7.9.3 Nanoparticle diameter equation

In order to better understand the meaning of the I_{rel} caused by the particles when moving through the pore, we developed an equation that establishes a relation between the I_{rel} and d. Before that, we needed to solve Eq. 24 in order of R_{PP}, as we needed to find an equation able to calculate the resistance of the pore when the particle is present, while not depending on d, which is given by:

$$I_{rel}(\%) = \left(\frac{R_{TP}}{R_{Total}} \times 100\right) - 100 \Leftrightarrow \frac{I_{rel}+100}{100} = \frac{R_{TP}}{R_{Total}} \Leftrightarrow \left(\frac{I_{rel}+100}{100}\right) R_{Total} = R_{TP}$$

$$\Leftrightarrow R_{PP} + R_{macro} + R_{micro} + R_C + R_{PC} + R_S = \left(\frac{I_{rel}+100}{100}\right) R_{Total} \Leftrightarrow$$

$$R_{PP} = \left(\frac{I_{rel}+100}{100}\right) R_{Total} - R_{macro} - R_{micro} - R_C - R_{PC} - R_S \quad (27)$$

In the case of double constriction channels Eq. 27 is transformed into:

$$R_{PP} = \left(\frac{I_{rel}+100}{100}\right) R_{Total} - \frac{R_P}{2} - R_{macro} - R_{micro} - R_C - R_{PC} - R_S \quad (28)$$

Thus, of all the equations, Eq. 26 was the only one that depended on d. However, as it is a 3rd order equation, we used Taylor series to solve Eq. 26 in function of d, as follows:

$$R_{PP}\sigma = f(d) = \left(\frac{d}{(W_P - d)d + W_P(H_P - d)} + \frac{L_P - d}{W_P H_P}\right)$$

$$\xrightarrow[Taylor]{} f(d_0) + \frac{f'(d_0)}{1!}(d-d_0) + \frac{f''(d_0)}{2!}(d-d_0)^2 + \frac{f'''(d_0)}{3!}(d-d_0)^3 \xrightarrow{d_0=0}$$

$$f(0) + f'(0)d + \frac{f''(0)}{2}d^2 + \frac{f'''(0)}{6}d^3 =$$

$$= \frac{L_P}{W_P H_P} + \left(\frac{W_P H_P + {d_0}^2}{\left(W_P H_P - {d_0}^2\right)^2} - \frac{1}{W_P H_P}\right)d + \left(\frac{2d_0\left({d_0}^2 + 3W_P H_P\right)}{\left(W_P H_P - {d_0}^2\right)^3}\right)\frac{d^2}{2} + \frac{6}{(W_P H_P)^2}\frac{d^3}{6} \xrightarrow{d_0=0} \Longleftrightarrow$$

$$R_{PP}\sigma = \frac{L_P}{W_P H_P} + \frac{d^3}{(W_P H_P)^2} \Leftrightarrow d = \sqrt[3]{(W_P H_P)^2 R_{PP}\sigma - L_P W_P H_P} \quad (29)$$

Using the I_{rel} calculated in Table 24 and Eq. 28 and 29 we obtained we R_{PP} and d values. No matter the value of the resistance in the pore when a particle is present for a high or low salt solution, the diameter of the particle is not influenced by the salt concentration, as it should (Table 25)

Table 25 – Expected NP diameter calculated from the relative current shift.

		I_{rel} (%)	R_{PP} (MΩ)		d (nm)
			LS	HS	
230 nm	Design 2	0,4215	0,60	0,25	237
	Design 5	0,0681	10,28	4,29	234
	Design 7	0,0364	0,60	0,25	237
	Design 11	0,3686	1,41	0,59	239
	Design 13	0,4729	1,41	0,59	239
252 nm	Design 2	0,5653	0,60	0,25	262
	Design 5	0,0906	10,29	4,29	258
	Design 7	0,0488	0,60	0,25	262
	Design 11	0,4966	1,42	0,59	264
	Design 13	0,6371	1,42	0,59	264
500 nm	Design 2	6,7688	0,98	0,41	598
	Design 5	0,8837	10,39	4,33	550
	Design 7	0,5848	0,98	0,41	598
	Design 12	1,4285	0,80	0,33	550

7.9.4 Electrical transport

One of the parameters to calculate related to the electrical transport is the field strength in the pore. This parameter can be obtained with the following equation:

$$E = \frac{J}{\sigma} = \frac{\frac{I}{A}}{\sigma} = \frac{I}{\sigma A} = \frac{V}{\sigma A R_P} \tag{30}$$

where J is the current density, I the current across the pore, A the cross sectional area of the pore, and V the voltage applied according to the salt concentration. In Table 26 are the values of the electric strength and electroosmotic velocity that result from Eq. 30 and Eq. 3, respectively.

Table 26 – Field strength and electroosmotic velocity for all designs according to salt concentration.

		R_P (MΩ)	$Area$ (m^2)	E (V/m)	v_{EOF} (m/s)
Low salt (137 mM PBS) **V = 100 mV**	Design 2	0,57	6,00 x 10^{-13}	2,00 x 10^{5}	3,00 x 10^{-3}
	Design 5	10,27	1,00 x 10^{-12}	6,67 x 10^{3}	1,00 x 10^{-4}
	Design 7	0,57	6,00 x 10^{-13}	2,00 x 10^{5}	3,00 x 10^{-3}
	Design 11	2,74	5,00 x 10^{-13}	5,00 x 10^{4}	7,50 x 10^{-4}
	Design 12	1,37	1,00 x 10^{-12}	5,00 x 10^{4}	7,50 x 10^{-4}
	Design 13	0,57	5,00 x 10^{-13}	1,00 x 10^{5}	1,50 x 10^{-3}
High salt (1 M PBS) **V = 30 mV**	Design 2	0,24	6,00 x 10^{-13}	6,00 x 10^{4}	9,00 x 10^{-4}
	Design 5	4,29	1,00 x 10^{-12}	2,00 x 10^{3}	3,00 x 10^{-5}
	Design 7	0,24	6,00 x 10^{-13}	6,00 x 10^{4}	9,00 x 10^{-4}
	Design 11	1,14	5,00 x 10^{-13}	1,50 x 10^{4}	2,25 x 10^{-4}
	Design 12	0,57	1,00 x 10^{-12}	1,50 x 10^{4}	2,25 x 10^{-4}
	Design 13	0,57	5,00 x 10^{-13}	3,00 x 10^{4}	4,50 x 10^{-4}

7.9.5 Hydrodynamic Resistance

As the electrical resistance, the total hydrodynamic resistance is the microfluidic device is given by the sum of the resistance in the macro, micro and nanochannels. The hydrodynamic resistance strongly depends on the geometry and viscosity of the fluid. Depending on the relation between the width and the height of a section, different expressions can be used to calculate the resistance of the pre-connector, the connector, the pore, the macrochannels and the microchannels. This happens since all these sections are either rectangular or squares. In the case of $w > h$, R_{hyd} is given by:

$$R_{hyd} = \frac{12}{1 - 0{,}63(h/w)} \eta L \frac{1}{h^3 w} \tag{31}$$

where w and h represent the width and the height, respectively, of the section being studied, and η the viscosity of the fluid. In this project we used the viscosity of water which is 8,90 x10^{-4} Pa·s. However, if $w < h$, then the R_{hyd} can be calculated with the following equation:

$$R_{hyd} = \frac{12}{1 - 0{,}63(w/h)} \eta L \frac{1}{w^3 h} \tag{32}$$

On the other hand, if $w = h$, R_{hyd} is given by:

$$R_{hyd} = 28{,}4 \eta L \frac{1}{w^4} \tag{33}$$

The only section of the entire microfluidic device that does not follow Eq. 31, 32 or 33, is the connector, as this section is a semi-circle. In this case the R_{hydC} is given by:

$$\int_0^R dR = \int_{W_P/\sqrt{2}}^{W_C/\sqrt{2}} \frac{12\eta}{h^3\left(\frac{\pi}{2}x - 0{,}63h\right)} dx \Rightarrow R_{hyd} = \frac{24\eta}{{H_C}^3\pi} \ln\left(\frac{\frac{\pi W_C}{2\sqrt{2}} - 0{,}63H_C}{\frac{\pi W_P}{2\sqrt{2}} - 0{,}63H_C}\right) \quad (34)$$

The results for the hydrodynamic resistance of the pore (R_{hydP}), the connector (R_{hydC}), the pre-connector (R_{hydPC}) and the separation (R_{hydS}) are in Table 27, along with the total hydrodynamic resistance of the nanochannel structure.

Table 27 – Hydrodynamic resistance of all the nanochannel components for each design.

	R_{hydP} (Pa·s/m^3)	R_{hydC} (Pa·s/m^3)	R_{hydPC} (Pa·s/m^3)	R_{hydS} (Pa·s/m^3)	$R_{hydNANO}$ (Pa·s/m^3)
Design 2	3,97 x 10^{16}	5,84 x 10^{16}	0	0	9,82 x 10^{16}
Design 5	3,79 x 10^{17}	0	0	0	3,79 x 10^{17}
Design 7	3,97 x 10^{16}	4,86 x 10^{16}	1,09 x 10^{18}	0	1,18 x 10^{18}
Design 11	2,49 x 10^{17}	8,89 x 10^{16}	2,26 x 10^{16}	6,40 x 10^{14}	3,62 x 10^{17}
Design 12	5,06 x 10^{16}	3,99 x 10^{16}	3,16 x 10^{16}	2,44 x 10^{14}	1,22 x 10^{17}
Design 13	1,25 x 10^{17}	4,44 x 10^{16}	4,55 x 10^{16}	0	2,15 x 10^{17}

The hydrodynamic resistance of the micro and macrochannels was also calculated using Eq. 31. The resistance of the macrochannels was 1,24 x 10^{14} Pa·s/m^3 and 1,19 x 10^{14} Pa·s/m^3 for the microchannels. Thus, as the calculated $R_{hydNANO}$ was much larger, the pressure used to obtain the flow rate in Table 9 was half of the applied value.

7.10 Biological Experiments

7.10.1 Human Serum

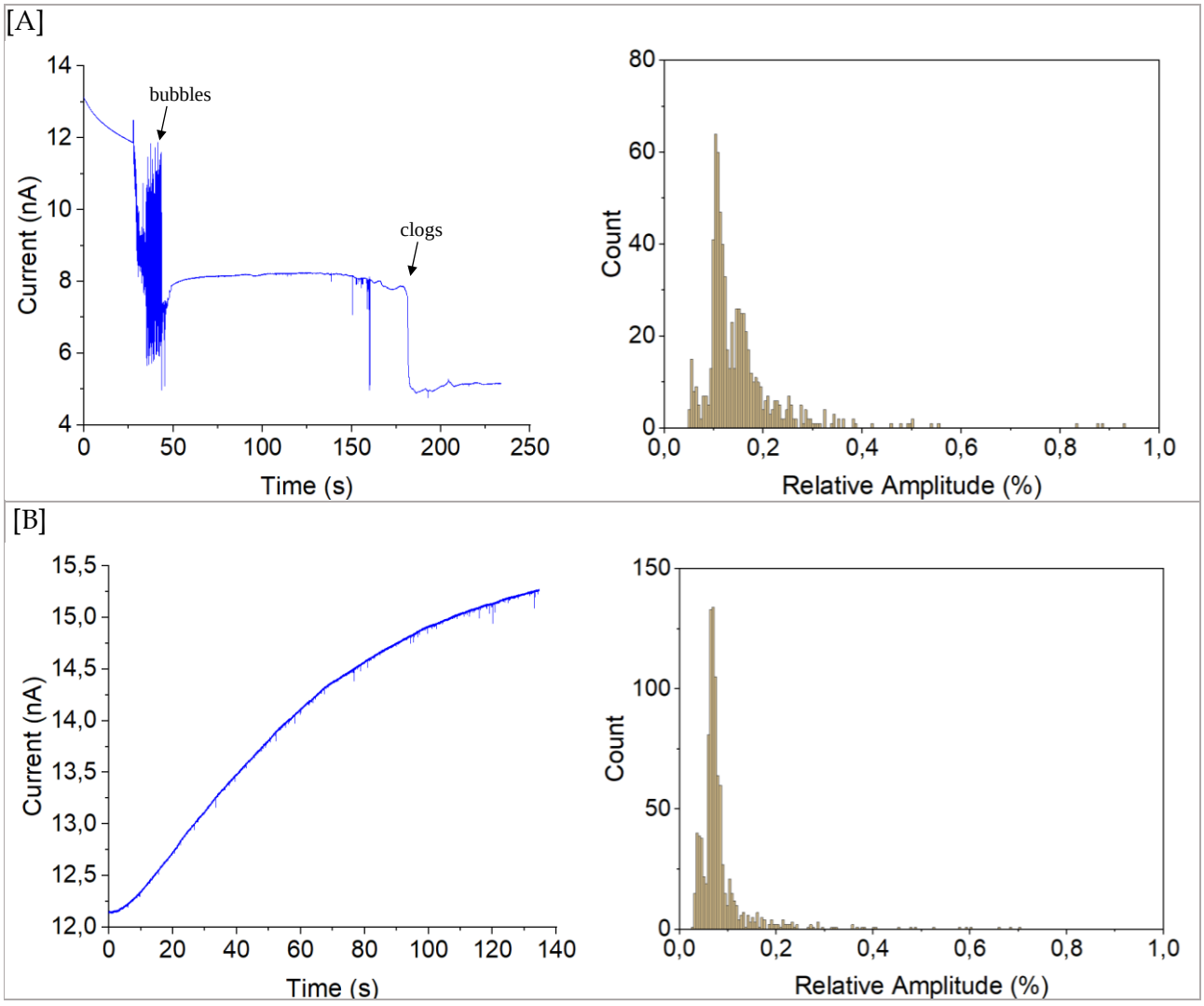

Figure 22 – Raw data and histograms of the Relative Amplitude Shift of the human serum sample in [A] Design 5 and [B] Design 2.

7.10.2 Purified EVs

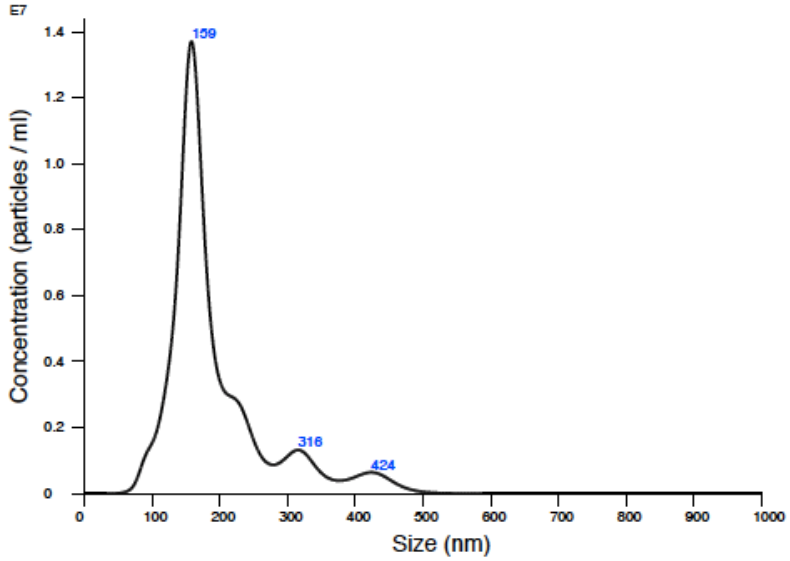

Figure 23 – Size distribution of the purified EVs sample, obtained by ultracentrifugation. This was provided by INL collaborators.

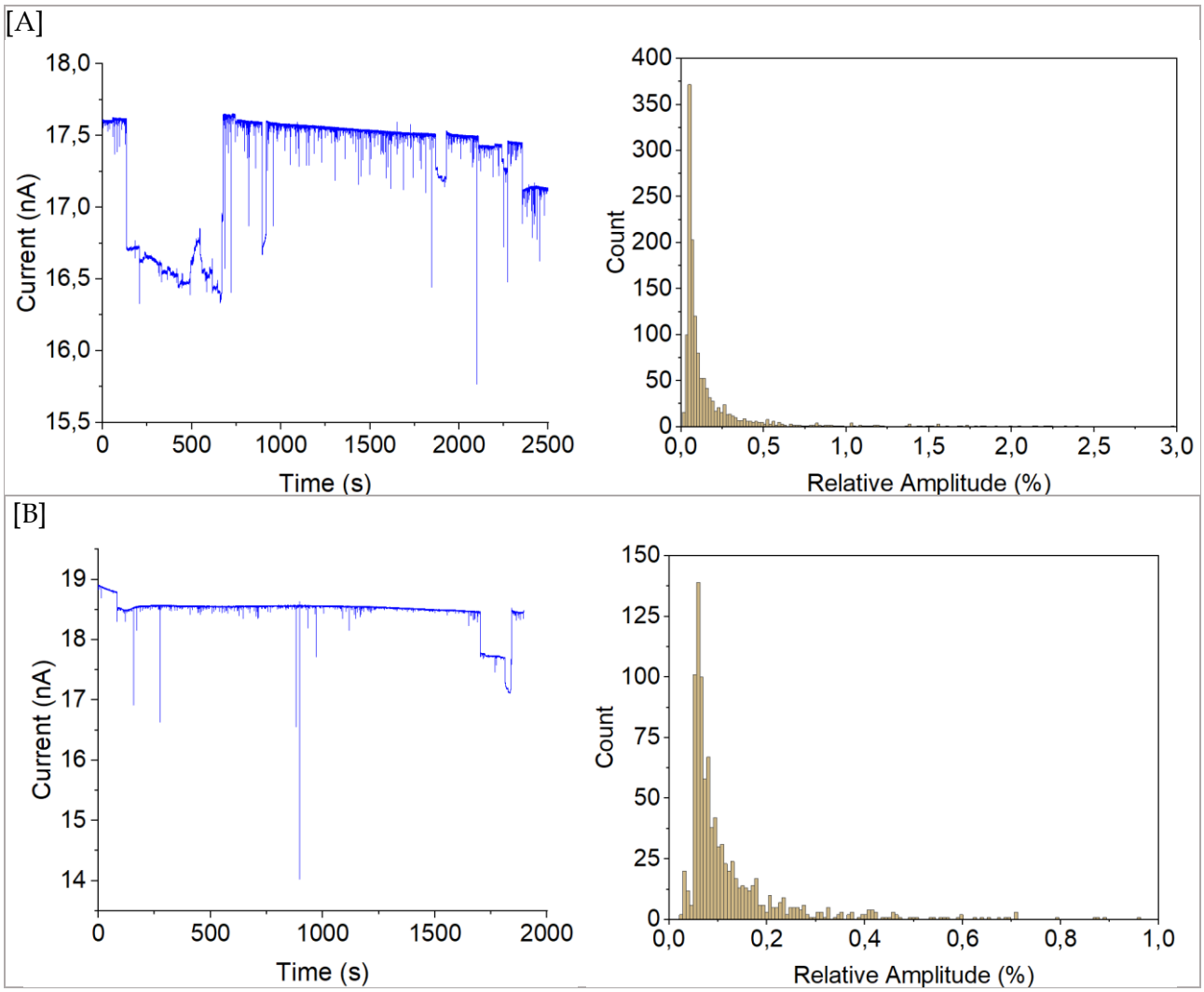

Figure 24 – Raw data and histograms of the Relative Amplitude Shift of the purified EVs sample in [A] Design 5 and [B] Design 2.

7.11 Patch-Clamp Amplifier vs. RPS Interface

In this project, we used Patch-Clamp amplifier to perform Resistive-Pulse Sensing, which allows us to detect current spikes with small amplitudes. However, Patch-Clamp amplifier is an expensive equipment. Thus, INL researchers developed an in-house sensor Interface to perform RPS. The most successful experiments on Patch-Clamp, for each channel type (smooth, single constriction, and double constriction channel), were remade on the Interface to evaluate and compare the ability of these devices to detect NPs. Examples of the spikes registered with each chip for each equipment are represented in Figure 25.

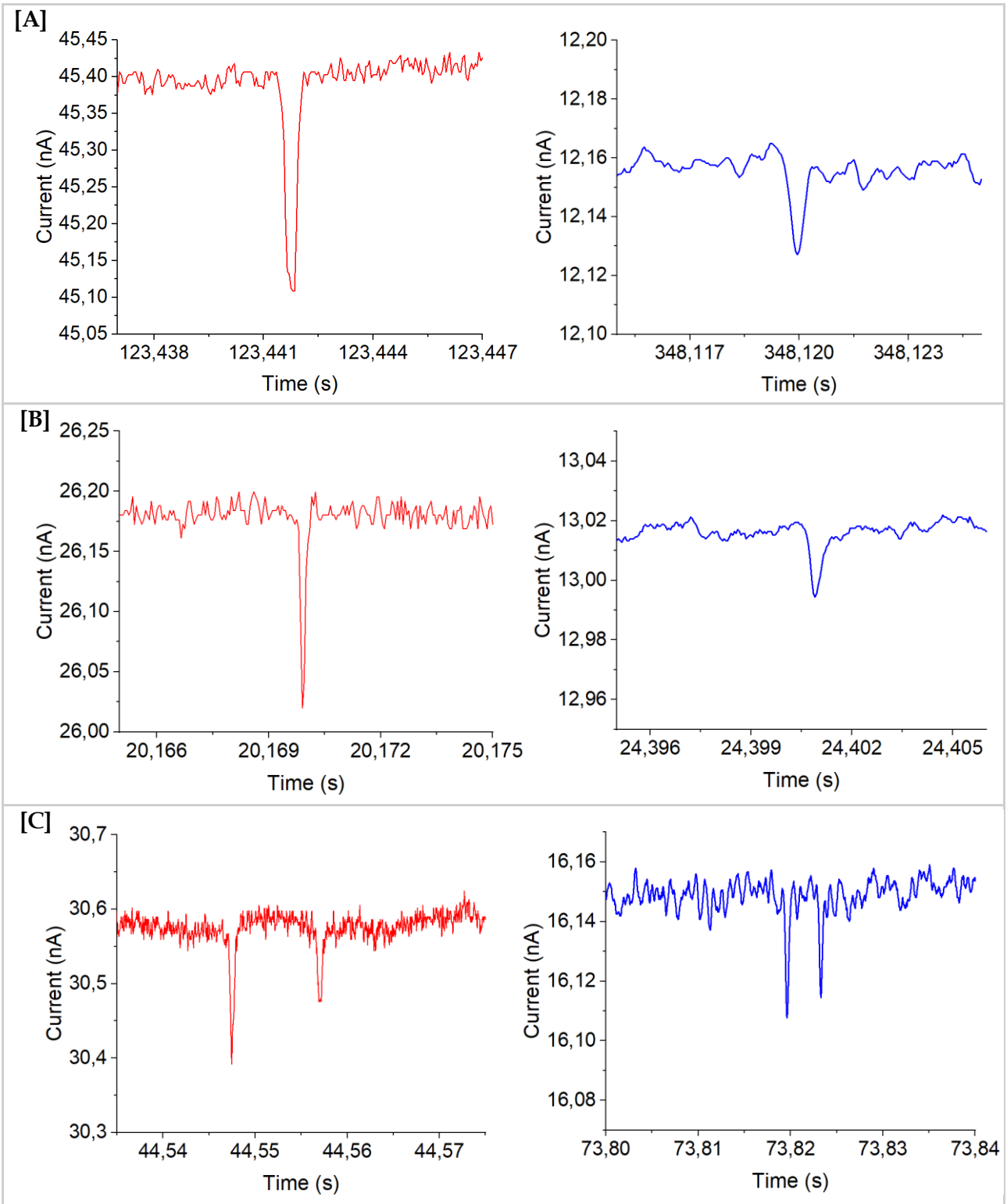

Figure 25 – Zoomed in spikes from the INL-made RPS interface (red) and Patch-Clamp amplifier (blue), for [A] a smooth channel, [B] a single constriction, and [C] a double constriction chip.

To properly establish a comparison between the two, the conditions used at Patch-Clamp (sampling rate, voltage, and solutions) were the same, when reproducing the experiments with the created RPS interface. The data collected from the three types of devices are represented in Table 28.

Table 28 – Parameter comparison between the RPS interface and Patch-Clamp the different channel types.

		RPS Interface	**Patch-Clamp**
Smooth Channel: Design 5 500 nm NPs 2,9 x10^9 (particles/mL) 1 M PBS V_{bias} = 30 mV	Spikes @ 200 mbar	1946	2870
	Frequency (Hz)	50,29	46,32
	Spike height (pA)	292,44 ± 40,43	35,67 ± 6,35
	Height variation (%)	13,83%	17,80%
	Baseline (pA)	(4,514 ± 0,051) x 10^4	(1,219 ± 0,013) x 10^4
	Noise (pA)	10,7	3,1
	Signal-to-noise ratio	27,3	11,3
Single Constriction: Design 13 230 nm NPs 2,5 x10^{10} (particles/mL) 0.137 M PBS V_{bias} = 100 mV	Spikes @ 50 mbar	2116	1326
	Frequency (Hz)	79,34	40,98
	Spike height (pA)	156,22 ± 89,97	26,40 ± 11,38
	Height variation (%)	57,59%	43,11%
	Baseline (pA)	(2,659 ± 0,050) x 10^4	(1,304 ± 0,005) x 10^4
	Noise (pA)	7,8	1,9
	Signal-to-noise ratio	20	14
Double Constriction: Design 11 230 nm NPs 2,5 x10^{10} (particles/mL) 1 M PBS V_{bias} = 30 mV	Spikes @ 100 mbar	370	381
	Frequency (Hz)	10,63	17,41
	Spike height (pA)	135,35 ± 45,11	40,92 ± 11,25
	Height variation (%)	33,33%	27,49%
	Baseline (pA)	(2,955 ± 0,105) x 10^4	(1,622 ± 0,006) x 10^4
	Noise (pA)	12,9	4,0
	Signal-to-noise ratio	10,5	10,2

In terms of quantity of detected spikes, and therefore, the number of particles passing through the channel, the RPS interface seems to be as capable of detecting them as Patch-Clamp, with an even higher number of spikes registered for the In-house made Interface at times.

Even though the standard deviation of the amplitude of the spikes seems smaller for Patch-Clamp, when analyzing the height variation instead, taken from the standard deviation over the mean height, it makes it noticeable how similar they are. The fact that both detection equipments have similar height variations, is an excellent indicator of how reliable the RPS Interface is for the characterization of nanoparticles.

The baseline of each experiment in the In-house made Interface is different from the one from Patch-Clamp. In the Interface, the baseline seems to have higher values and an increased variation compared to Patch-Clamp, meaning more signal drifting.

The most significant difference between the two pieces of equipment is the noise registered. The noise measured with the RPS Interface can be three or more times higher than the noise registered by Patch-Clamp, limiting the detection of smaller current spikes caused by smaller NPs.

However, there are other parameters that should be considered when comparing both detection

equipments, such as signal-to-noise ratio, the cut-off frequency of these interfaces, and the shielding differences. Regarding the signal-to-noise ratio, the RPS interface seems to have higher values, meaning this interface has more signal information corresponding to spikes than noise. This could be explained by the cut-off frequencies of the two, for the RPS interface it is 4 kHz and 1 kHz for Patch-Clamp, which means that the RPS interface has a bigger bandwidth than Patch-Clamp. Another significant difference between the two is the copper box used as a shield from external interferences in the RPS interface set-up, the Patch-Clamp used did not have such shielding present.

Table 29 – Comparison between Patch-Clamp and In-house made RPS Interface success rate.

Channel Type	Solution	Success rate @ Patch-Clamp	Success rate @ In-house Interface
Smooth Channel (Design 5)	500 nm NPs 2,9 x10^{9} (particles/mL) 1 M PBS	62,50% (N=8)	37,50% (N=8)
Single Constriction (Design 13)	230 nm NPs 2,5 x10^{10} (particles/mL) 0.137 M PBS	85,71% (N=7)	50,00% (N=8)
Double Constriction (Design 11)	230 nm NPs 2,5 x10^{10} (particles/mL) 1 M PBS	71,43% (N=7)	42,86% (N=7)

Lastly, when comparing the direct success rate (Table 29), for the same combination of solutions used with chip design in the different types of equipment, the In-house made RPS Interface has a lower success rate. This lower success rate can be explained by the fact that this interface was not made to use such low bias voltage values as we did, as it was made to rely more on electrical transport, which strongly depends on the bias voltage applied, as mentioned in section 2.2.1 of the Introduction. The detection of those solutions in these channel types increases 1,7 times when using Patch-Clamp instead of the Interface.

Overall, the Interface achieves its purpose and can detect current spikes successfully. However, it is a trade-off choosing to work with the developed RPS Interface instead of Patch-Clamp amplifier. It is all about compromising higher noise and more baseline drift for cheaper equipment, as it is the current bottleneck of this in-house-made Interface. This means that smaller spikes may not be detected and lost in the noise, leading to inaccurate quantification of NPs passing through the channel. Nevertheless, the developed RPS interface is as good as Patch-Clamp Amplifier and is a reliable analysis interface.

2021

MADALENA ROSA CORREIA CALADO

Pressure-Driven Resistive Pulse Nanopore Sensing for the Characterization of Extracellular Vesicles

NOVA SCHOOL OF SCIENCE & TECHNOLOGY